Numerical Modelling and Experiments of Silicon Electrodeposition by Solid Oxide Membrane - Molten Salt Electrolysis

A Dissertation presented in partial fulfilment of the requirements for the degree of
Doctor of Philosophy in Materials Science and Engineering
at Worcester Polytechnic Institute
Worcester, Massachusetts, April 2023

by
Aditya Moudgal
Advisor: Dr Adam Clayton Powell, IV

Committee
Chair: Adam C. Powell, IV, Worcester Polytechnic Institute
Brajendra Mishra, Worcester Polytechnic Institute
Yu Zhong, Worcester Polytechnic Institute
Uday Pal, Boston University
Matthew Earlam, Argonne National Laboratory

Abstract

The demand for cost-effective and sustainable solar energy has spurred the need for cheaper, cleaner solar panels with low carbon footprints. One critical component of solar panels is silicon, whose energy intensive, multistep manufacturing process has been an obstacle in achieving low stable prices. This project explores mathematical modelling and experimentation methods of achieving high purity solar grade silicon through solid oxide membrane (SOM) – molten salt electrolysis in a single step with no carbon by-product. SOM electrolysis has been previously employed in the production of magnesium, titanium, and tantalum.

In this work, the anodic primary, secondary, and tertiary current density distributions are modelled. The models used a simplified unit of a large-scale cell with an electrolyte conductivity value of 438 S m^{-1} with a flux composition of MgF_2 – CaF_2 – CaO – Y_2O_3 – SiO_2. The anodic current density distribution was found to be between 0.5 ~ 1 A cm^{-2}. An optimal cathodic thickness beyond which current density changes minimally was found to be 6 cm. The magnetohydrodynamic (MHD) effects due to current flowing through the conductor are modelled and show a very slow flow rate in the electrolyte compared to an analytical calculation. Lab scale experimental work shows pure silicon deposits in the flux using a solid silicon cathode at an operating temperature of 1100^0C.

Acknowledgements

This dissertation would not be possible without the guidance of my advisor Prof. Adam Clayton Powell, IV. I would like to thank him for giving me the opportunity to be his first doctoral student at WPI. His enthusiasm, insight and patience has been invaluable in completion of this dissertation. Doing a PhD is hard but doing a PhD during the COVID-19 global pandemic was a whole new ball game. I would like to thank him for his immense understanding and faith in me during those times. I would like to also thank my committee members, Prof. Yu Zhong (WPI), Prof. Brajendra Mishra (WPI), Prof. Uday Pal (Boston University) and Matt Earlam (Argonne National Laboratory) for their support. I would especially like to acknowledge Prof. Pal and his student Haoxuan Yan for their discussions and suggestions towards the completion of the project.

I would be remiss if I did not thank the administrative department in the Materials Engineering Program here at WPI. I would like to specially acknowledge Rita Shilansky, GlorieAnn Minnich, Maureen Plunkett, and Shelly Woods in all their help. None of the experimental work would be possible without the help of the WPI manufacturing labs and the help of Toby Bergstrom, James Loiselle, Ian Anderson, and Joel Harris. A special shout out to Michael Collins, lab manager of the Metal Processing Institute for help in setting up furnaces and equipment in our lab space.

I would like to acknowledge all the undergraduate Major Qualifying Project teams I have worked with over the last four years. Thank you to Sarat Buasai, Alex McMohan, Yi Je Wu, Vicky Lu, Jacob Hazerian, Ariana Li, Alex Alonzo, Peter

Catalino, Tyler Melo, Andrew Charlebois, and Evan Costa for their collaboration and efforts.

I would also like to acknowledge the support of teammates in the Energy Metals Research Group and friends over the last four years. In no particular order, thank you to Dr Sathwik Bharadwaj, Prajwal Bharadwaj, Rahul Jakhmola, Ashish Gurung, Dr Hyunsoo Jin, Dr Yao Xu, Dr Mark Strauss, Dr Debanik Das, Qingli Ding, Mahya Shahabi, Yash Yadati, Anurag Bhattacharjee, Dr Mohammad Asadikya, Gabriel Espinosa, Lucian Wallace, Alexander Wadsworth, Douglas Moore, Armaghan Telgerafchi, Dr Kübra Karayağız, Akanksha Gupta, Dr Manish Sinha, Chaitanya Ruhatiya, Celso de Cabo, Ashay Aswale, Chinenye Chinwego, Daniel McArthur, Zujian Tang, Madison Rutherford, Noelle Rakotondravony, and Fatou Diop. I apologize if I have inadvertently omitted any names, but please know that your support has not gone unnoticed. Each one of you has played a crucial role in my success, and I am grateful for your time and support.

Lastly, I would like to thank my parents Dr G.V. Giri and Dr Shubha Rao and my extended family for their love and support.

Table of Contents

List of Figures

List of Tables

Chapter 1 - Introduction

1.1 Project Background

Silicon is an important industrial metal that has seen widespread usage and adoption in the solar energy, electronics, and metallurgical industries. It plays an important role especially in the solar industry where polysilicon and mono-silicon based solar cells dominate the market due to abundance of silicon availability, low cost, and high practical efficiency, and look to stay in the market in the near future (Woodhouse et al., 2019). Silicon modules are expected to last 25 years or more and retain 80% efficiency (*Solar Photovoltaic Cell Basics*, n.d.). Therefore, having a clean, low cost, source of silicon is necessary to advance wider usage of solar technology at competitive costs.

An installed system cost analysis by NREL (*Solar Manufacturing Cost Analysis*, n.d.) has shown that the price of solar modules has been constantly decreasing since 2010 and for further decrease in the price per kilo watt hour (kWh) the cost of silicon also needs to be competitive. But current manufacturing of solar grade silicon through the Siemens process is energy intensive, unsafe, and environmentally harmful due to a carbon dioxide by-product (Osborne, 2014). Combined with uncertainty and volatility in silicon prices (*Polysilicon Price Reaches $39.3/Kg — the Highest since 2011*, 2022) newer methods of refining silicon to solar grades need to have been explored (Chigondo, 2018).

To produce solar grade silicon, inexpensive and 99.6-99.8% pure silica is carbothermically reduced to form metallurgical grade silicon which is about 98% pure.

$$SiO_2 + C \rightarrow Si + CO_x$$

This metallurgical grade silicon is further refined into solar grade silicon by hydro-chlorination using hydrochloric acid, followed by distillation to form purified trichlorosilane which is an intermediate product. This is then deposited by chemical vapour deposition in bell jars as shown in the flowsheet graphically in Figure 1 (Maurits, 2014).

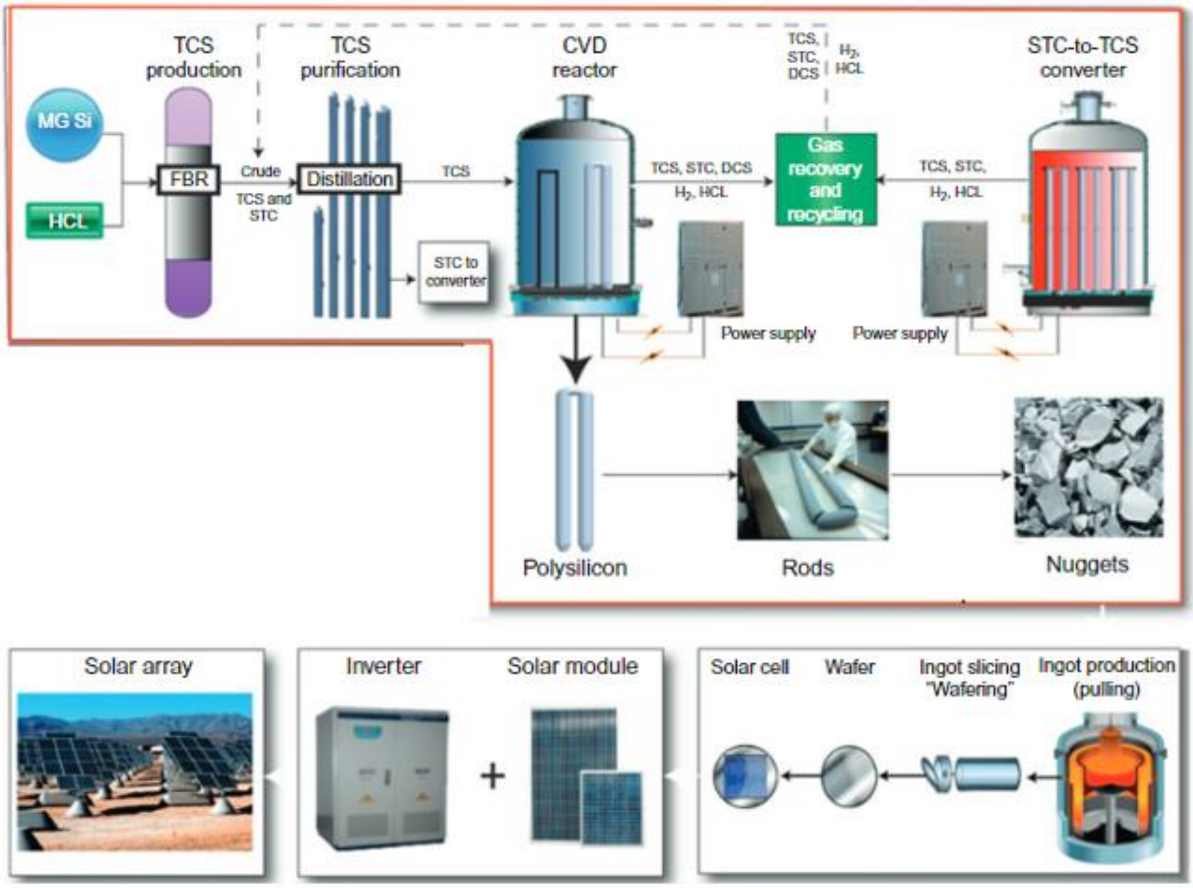

Figure 1: Siemens Process of Refining Silicon

Like reduction of aluminium smelting from bauxite using molten salt electrolysis, there have been various attempts to reduce silica to silicon electrochemically. Reduction of silicon from molten salts shows promise due to low energy expenditure and cost. Production of silicon from molten salt electrolysis can be done using either chloride or fluoride melts or a combination of both (Nohira, 2014; Padamata & Saevarsdottir, 2023; Yasuda & Nohira, 2022). All three types of melts have been investigated and have shown promise. The scientific challenge that remains during deposition is salt entrapment in non-planar and non-uniform growth of the deposit (Elwell & Rao, 1988) and a high viscosity of the melt. To address these challenges, a new novel flux was developed by (Villalón Jr, 2018). This flux consists of a two-salt fluoride base of magnesium fluoride and calcium fluoride (MgF_2-CaF_2) and calcium oxide, yttrium fluoride and silica (CaO-YF_3-SiO_2). It has low volatility of <0.1 µg cm^{-2} s^{-1}, low viscosity of < 5 mPa*s, high ionic conductivity of > 4 S cm^{-1} and good SiO_2 solubility of > 5 wt.%.

It was demonstrated by Villalón et al. that the salt mentioned above can be used to deposit silicon using two reactive cathodes i.e., molybdenum (Mo) and tin (Sn). The challenge here lies in commercialization of a suitable cathode. The motivation to use a solid cathode in this project is to avoid introducing impurities as seen in the Mo and Sn, though it requires that one overcome the challenges of salt entrapment by solidification instabilities, particularly dendrites. Periodic reversal of current can also address the challenge of non-planar and non-uniform growth in the melt. The salt electrolyte composition is also compatible with yttria-stabilised zirconia solid oxide membrane (SOM) anodes, which would reduce introducing impurities and silicon carbide formation with a traditional carbon anode.

The progress made in this project could enable production of silicon at similarly low cost as, and on the scale of the Hall-Héroult process used to produce aluminium. A decrease in cost and energy increases the scale and the goal towards wider availability of cheap, high purity silicon.

1.2 Project Objectives

The main purpose of this project is to model a large-scale electrochemical cell having a solid oxide membrane as an anode and correlate the models with laboratory scale experiments. This is part of a larger NSF project that consists of four parts being thermodynamic and microscale density functional theory modelling of the salt, experimental validation of the process, macroscale finite element modelling, and mesoscale phase field modelling. Macroscopic scale computer mathematical models help in understanding the physics and cutting down on experimentation, cost, and development time. The numerical modelling of the anodic current density distribution, effect of magnetic fields causing magnetohydrodynamic (MHD) effects and heat transfer in a large-scale cell can help understand the dynamics of silicon growth and conditions needed to make the process economically viable. MHD is particularly important with a SOM anode because unlike a carbon anode which would provide gas lift stirring from CO_2 bubbles, MHD is the primary stirring mechanism with SOM. The governing equations for these phenomena are standard equations such as the Nernst-Planck-Poisson equation, the Navier-Stokes equation, and Maxwell’s equations, plus interaction terms such as Joule heating and Lorentz force. The challenge here lies in coupling these equations with the appropriate boundary conditions.

1.3 Dissertation Overview

Chapter 1 gives a brief introduction to the vision of the project and what the dissertation hopes to achieve.

Chapter 2 is a brief literature survey of the current state of the art to produce silicon electrochemically via experiments. Various methodologies from the past to the most recent are discussed. A brief introduction to solid oxide membrane processing is given. A brief techno-economic model describes the viability of the process.

Chapter 3 talks about the numerical models developed for the solid oxide membrane electrolysis of silicon. It describes the basic equations, boundary conditions and the application of these equations using the commercial finite element analysis software COMSOL. These numerical models show results that can help with scaling up the process and discuss what the optimal conditions would be for good quality grain growth.

Chapter 4 describes the experimental efforts to produce high quality pure silicon deposits using a solid cathode. The merits of the system currently being used and a method to scale up the process are described.

Chapter 5 summarises the dissertation and discusses the merits, limitations and future work needed to further the science.

Chapter 2 - Literature Review and Techno-Economic Model

2.1 Experimental State of Art

Silicon electrodeposition is a promising method for oxide reduction as it uses the cleanest reductant viz. the electron (Maldonado, 2020). The process can be easily scaled based on the Hall-Héroult process for the production of aluminium which is the commercial gold standard in fused salt electrolysis (Kvande, 2014). Though various attempts have been made as early as 1865 (Nohira, 2014) to produce silicon by molten salt electrolysis, large scale production has not been achieved. An analysis in 2020 concluded that by the end of 2019 more than 0.5 terawatts of power was generated using photovoltaics (Wilson et al., 2020). Therefore, due to price volatility, demand for clean power and the widespread usage of crystalline silicon still dominating the market (*Photovoltaics Report - Fraunhofer ISE*, n.d.), we need alternative methods to refine silicon.

The advantages of molten salt electrolysis are that silicon is deposited on the cathode at a lower potential that the contents of the electrolyte. Therefore, by controlling the cell voltage, it is easy to control the dissociation potentials and get a high purity product. Early attempts to imitate the Hall-Héroult process by Monier and Giacometti by dissolving SiO_2 in cryolite (Na_3AlF_6) at 1000^0C yielded anywhere between 99.7 - 99.99% pure product (Monnier & Giacometti, 1964). But, direct reduction of quartzite to silicon using different types of molten salts in a single step saw a lot of investigations in the 1980’s and 1990’s (Yasuda & Nohira, 2022). Various cathode materials have been utilised, including electro-deoxidation cathodes, reactive cathodes of potassium fluorosilicate (K_2SiF_6), and liquid aluminium, copper, nickel, gallium, and zinc to avoid SiC formation. However, this approach has not been commercialised due to challenges including low SiO_2 solubility in molten chlorides, side-reactions that generate volatile $SiCl_4$ and SiF_4, high viscosity and low conductivity caused by silicate polymerization, contamination by carbon anodes and their impurities, and trapped salts in the final product (Bøe et al., 1971, 1972; Cohen, 1977; Elwell & Rao, 1988; Grjotheim et al., 1971; Haarberg et al., 2019a, 2019b; Jin et al., 2004; Juzeliunas, 2022; Ma et al., 2019; Moore et al., 1997; Oishi et al., 2011; Yasuda et al., 2005)

Solid oxide membrane (SOM) electrolysis is an emerging technology for producing silicon and other metals in a more environmentally friendly and energy-efficient manner compared to traditional methods, such as the carbothermic reduction (Pal & Powell, 2007). In the context of silicon production, solid oxide membrane electrolysis involves the electrochemical reduction of silicon dioxide at high temperatures, typically between 960°C and 1200°C.

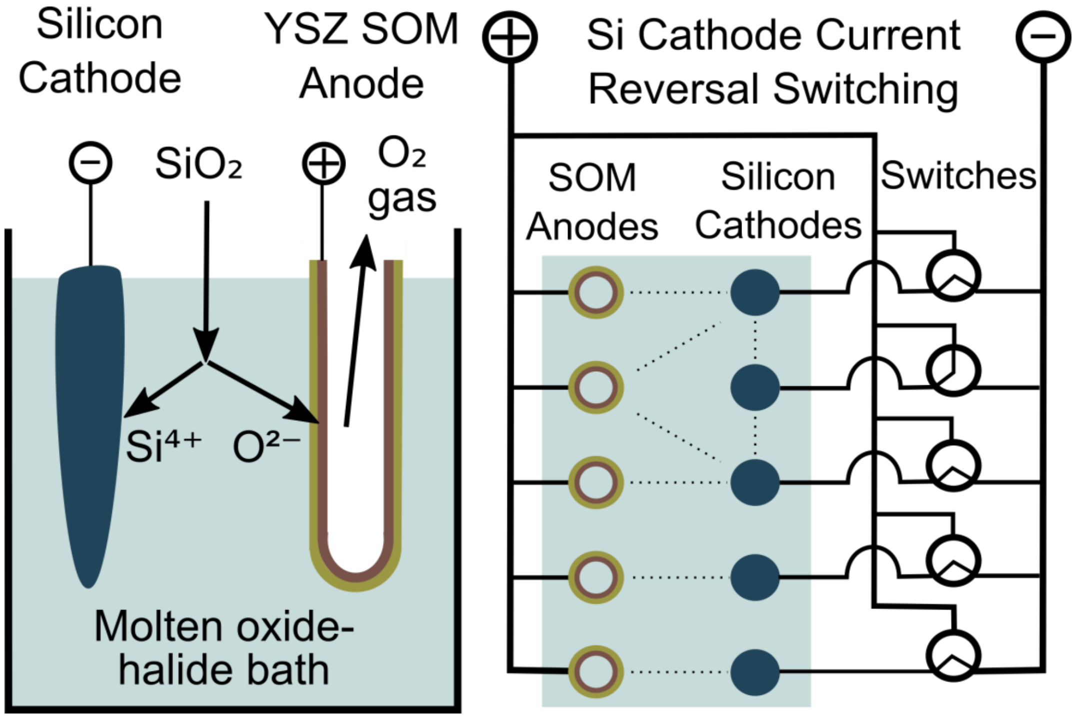

Figure 2: a. SOM electrolysis cell (left). b. Cell with a periodic pulse reverse electroplating setup to mitigate dendrite formation (right)

The process consists of the following key components:

Solid electrolyte: A dense, oxygen-ion conducting ceramic material, usually yttria-stabilised zirconia (YSZ), serves as the solid electrolyte. It separates the silicon dioxide feed material from the anode and allows oxygen ions to pass through it selectively.

Cathode: The cathode is typically a conductive metal or metal alloy, such as molybdenum, which was in contact with the solid electrolyte in previous iterations of experiments. The cathode is where the reduction of silica takes place, resulting in the formation of silicon metal.

Anode: The anode is an inert material, like silver. Previously an inert current collector such as lanthanum strontium manganite (LSM) (Guan et al., 2013) has been used in contact with silver placed in contact with the solid electrolyte. At the anode, oxygen ions are oxidised to form oxygen gas, which is released as a by-product.

External circuit: An external voltage is applied between the anode and the cathode, driving the electrochemical reduction process.

The overall process for silicon can be described by the following reactions:

At the cathode:

$$SiO_4^{4-} + 4e^- \rightarrow Si + 2O^{2-}$$

At the anode:

$$2O^{2-} \rightarrow O_2 + 4e^-$$

Net reaction:

$$SiO_2 \rightarrow Si + O_2$$

The advantages of solid oxide membrane electrolysis of silicon include:

Energy efficiency: The process requires less energy than traditional methods, as it is single step, operates at lower temperatures than carbothermic reduction, and does not require the use of carbon.

Environmental benefits: The process generates oxygen as the only by-product, which is less harmful to the environment compared to the greenhouse gases produced in the carbothermic reduction process.

Versatility: The SOM process can be applied to produce other metals, such as aluminium, magnesium (Krishnan, 2006), tantalum, and titanium, by altering the feed materials and process conditions.

2.2 Techno-economic Analysis

Based on the principle of cost-informed discovery (Spatocco & Sadoway, 2015) this project was evaluated for its commercialisation potential through the northeast regional NSF I-Corps program. Interviews were conducted with experts and stakeholders and a techno-economic analysis was conducted by (Buasai et al., 2020; Hazerjian et al., 2021; Moudgal et al., 2021). The cost analysis employs the techno-economic evaluation spreadsheet v1.0 from the US Department of Energy's ARPA-E METALS Tool (Matuszak, 2013).

This evaluation tool encompasses:

- A mass balance computation, determining element-wise balances by accounting for raw material expenses and revenue from sales.
- Capital expenditure considerations, including equipment and associated utility expenses.
- Projections for additional operating costs.

- Estimation of overall energy consumption and direct CO_2 emissions per unit of metal generated.
- A financial model incorporating return on investment.

In this investigation, a linear equation system is integrated into the ARPA-E METALS Tool, along with a solution for ascertaining the compositions and flow rates of five interconnected streams: input raw material and bath, and output silicon, oxygen, and bath. This leads to an input-output balance for all 13 model elements, which is accurate within the spreadsheet's precision constraints, as corroborated by the initial spreadsheet's streams and composition sheets. The mass balance utilises silica raw material purity and pricing data (Vatalis et al., 2015). It postulates that alumina is the primary silica impurity and introduces new CaF_2, MgF_2, CaO, and Y_2O_3 to maintain a low alumina concentration in the bath. Anodes are not incorporated into the mass balance at this stage.

Furthermore, this study extends the ARPA-E METALS Tool by incorporating an energy balance following (Powell & Pati, 2012), which sums up the reduction potential and ohmic overpotentials to approximate the electrical energy input per coulomb of charge transmitted as shown below.

$$V = -(\Delta G/ n F) + (\sum (J_i L_i) / \sigma_i) + 2 (\sqrt{L_{el}} T\Delta T)$$

where ΔG = free energy of formation of SiO_2

n = number of electrons transferred in the reaction.

F = Faraday's constant

J_i = current density

L_i = thickness of component i

σ_i = resistivity

L_{el} = Wiedemann-Franz constant

T = absolute temperature

ΔT = temperature difference

The thermodynamic data for this equation can be obtained from NIST JANAF tables (Chase, 1996), temperature dependent conductivity of the flux and YSZ membrane from (Krishnan, 2006) and (Villalón Jr, 2018). The cathodic resistance does not feature in this calculation.

The energy balance computes the thermal requirement per kg of silicon product, taking the enthalpy of formation of SiO_2, the total electrical and thermal losses via the leads, and the energy needed to heat SiO_2 raw material to cell temperature. It is defined below as

$$\text{Energy} = -\Delta H_f + 4\,n\,F\,(\sqrt{}\,L_{el}\,T\,\Delta T) + \int C_p\,dT$$

In a self-heating cell, the thermal energy consumption should be less than that of electrical input as determined by the energy balance equation with any surplus energy being dissipated as heat. When comparing the process to the Hall - Héroult cell with inert anodes, the theoretical energy usage for silicon is 9.02 kWh kg^{-1}, which is higher than the 8.62 kWh kg^{-1} for aluminium. The production at optimal Faradaic efficiency is 262 g kAh^{-1} for silicon compared to 336 g kAh^{-1} for aluminium, a difference of about 22%, demonstrating their high similarity.

The cost model incorporates raw material prices of $150/t for 99.8% pure SiO_2, 37 $150 t^{-1} for CaO, $400 t^{-1} for CaF_2, $1000 t^{-1} for MgF_2, and $5000 t^{-1} for Y_2O_3, which is about half as expensive per unit of yttrium as YF_3 and electricity prices of 30 MW h^{-1} from various aluminium plants. To estimate the capital costs, a novel capital cost model by (Stinn & Allanore, 2020) is used which considers electrolysis temperature, production capacity, and other relevant electrochemical operating parameters. The model's estimates have been verified by applying them to cases in the paper, as well as by considering a rough estimate of current costs for a new Hall- Héroult cell and equipment. To estimate labour costs, data from an interview with a Senior Potline Process Engineer at Century Aluminium smelter in South Carolina was used. This model does not include the SOM costs. It also does not include additional revenue due to sale of pure oxygen produced through this process as the sale of oxygen is very location specific.

2.3 Techno-economic Analysis Results

Figure 3 below presents the outcomes of the mass and energy balances. The output flow rate is marginally higher than the input flow rate due to the integration of silica and alumina from the raw material. For every 100 kg of Si produced, 215.4 kg of SiO_2 is required. Using 99.8% pure SiO_2 containing 0.1 wt.% Al_2O_3, the bath cost to maintain the alumina concentration in the electrolyte at 1 wt.% (an approximation for the required bath purity to achieve high product purity) constitutes about 59% of the SiO_2 cost. Table 1 below demonstrates the flow rate and cost of each material, excluding anode materials, with a total annual cost of just over $82 million.

It is feasible to separate aluminium from waste fluoride electrolyte through physical, electrochemical, or hydrometallurgical methods, and recycle the bath at a lower cost than acquiring new material; this analysis does not consider any such activities. The energy balance reveals that the high resistance in the molten salt electrolyte and YSZ solid electrolyte results in a cell potential of 3 V to 5 V, and excess thermal energy for a self-heating cell at temperatures below 1200°C. At 1100°C, the total cell voltage is estimated to be 3.37 V, not accounting for the concentration polarizations in the molten salt boundary layers adjacent to the anode and cathode.

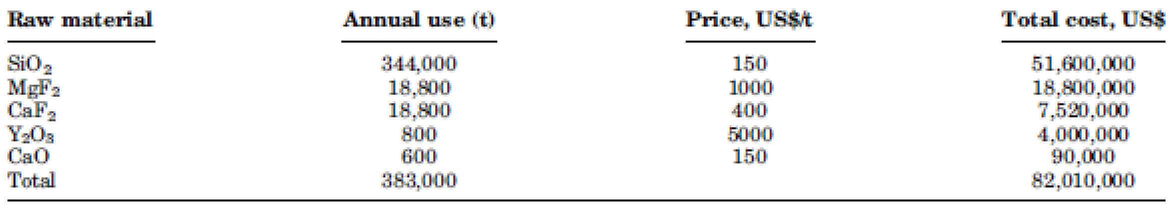

Raw material	**Annual use (t)**	**Price, US$/t**	**Total cost, US$**
SiO_2	344,000	150	51,600,000
MgF_2	18,800	1000	18,800,000
CaF_2	18,800	400	7,520,000
Y_2O_3	800	5000	4,000,000
CaO	600	150	90,000
Total	383,000		82,010,000

Table 1: Cost of material per annum

The plant's electrical energy consumption is 2.29 TWh a^{-1}, at a cost of $68.6 million a^{-1}. Comparing this to an aluminium plant, annual non-electricity utility costs are approximately $13 million a^{-1}, which is added to the utility costs in the estimation. For a 160,000 t a^{-1} silicon plant, the estimated labour cost for 600 operators and 50 overhead workers, costing \$92,634 a^{-1} and \$63,800 a^{-1}, respectively, amounts to \$58.8 million a^{-1}. Other overhead and miscellaneous costs are estimated at 25% of raw material, electricity and other utility, and labour costs, totalling \$59.6 million a^{-1}. The estimated annual operating costs are thus \$279.0 million a^{-1}, i.e., \$1.74 kg^{-1} silicon product.

The total capital cost estimated using the cost model developed by Stinn and Allanore is \$1.68 billion, which is around \$10,500 per t/a of production. This estimation is independent of aluminium production by Hall-Héroult cells and only relies on the Si-related operating parameters. The finance model assumes that 10% of this capital investment is spent in year 1, 60% in year 2, and 30% in year 3. Production reaches 50% of capacity in years 3 and 4, and 100% starting in year 5.

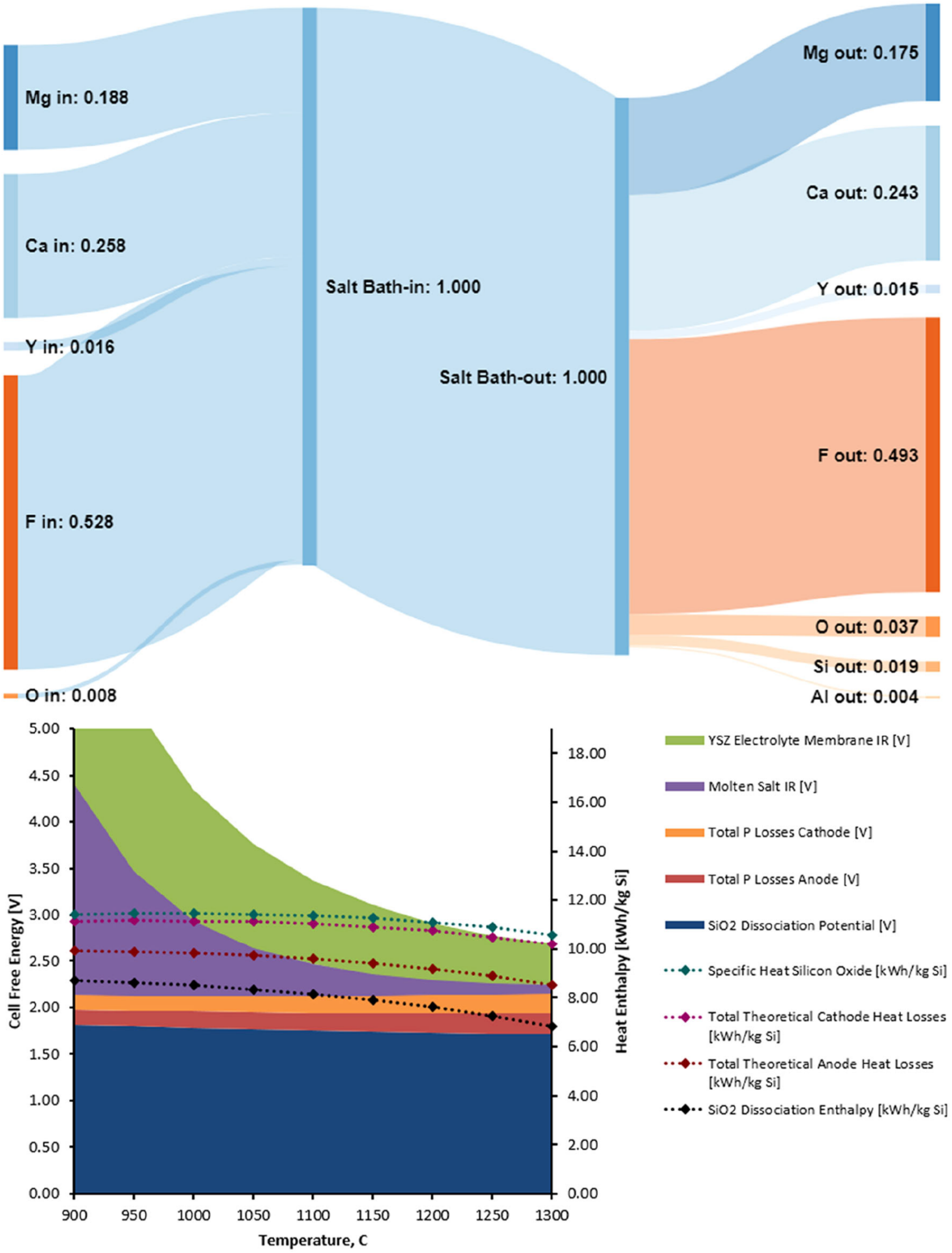

Figure 3: Techno-economic model showing material flow, energy, and enthalpy calculations.

Chapter 3 - Macroscale Modelling

In this section, the theoretical concepts and workings of a large-scale silicon electrochemical cell based on the Hall-Héroult cell, and its modelling are described. The primary, secondary and tertiary current density distribution equations and the magnetohydrodynamics (MHD) of the cell with its respective equations and simulations are described with results and discussions.

3.1 Current Density Distribution

Current density distribution is the variation of local current density during electrodeposition along a solid electrode’s surface. The current density distribution determines the morphology of a deposit in an electrochemical cell. For even deposition of material, the various factors that can affect the deposit are geometry, conductivity of electrolyte and electrodes, activation overpotential (kinetics), concentration overpotential (mass transport) and hydrodynamics of the cell (Ibl, 1983).

3.1.1 Nernst-Planck Equation

The Nernst - Planck equation is a conservation equation which describes ion transport phenomena in a wide range of systems including electrochemical systems. The equation is dependent on the number of ionic species of the system. The Nernst-Planck equation can be used to model current density in electrochemical cells by considering a generalised form and subsequently making certain assumptions of the field variables.

Consider a mass conservation equation,

$$(\partial C_i / \partial t) + \nabla . N_i = R_{i,\ tot}$$

where N_i = total flux of species i in mol $m^{-2}\ s^{-1}$

The Nernst-Planck equation describes flux N_i of any ion and is governed by diffusion, migration, and convection,

$$N_i = -D_i \nabla c_i - z_i u_{m,i} F c_i \nabla \phi_l + c_i u$$

where c_i = concentration of the ion in mol m^{-3}

D_i = diffusion constant in $m^2\ s^{-1}$

$u_{m,i}$ = mobility of the ion in s mol kg^{-1}

ϕ_l = electrolyte potential

u = velocity vector in m s^{-1}

F = Faraday's constant viz. 96485 C mol^{-1}

The term $(-D_i \nabla c_i - z_i u_{m,i} F c_i \nabla \phi_l)$ can be defined as the molar flux J_i.

For a flux which is ionic in nature, the current density is the sum of all fluxes of ions viz.

$$i_l = F \sum_i (z_i N_i)$$

where i_l = current density vector in flux in A m^{-2}

with the remaining terms described above.

A generalised current density can be obtained by substitution of the Nernst-Planck equation in the current density.

$$i_l = - F (\nabla \sum_i z_i D_i c_i) - F^2 \nabla \phi_l \sum_i z_i^2 u_{m,i} c_i + u F \sum_i z_i c_i$$

with conservation of current being $\nabla . i_l = Q_l$

3.1.2 Primary Current Density Distribution

The primary current density distribution of a cell is defined as the ohmic resistance of the cell. The ohmic resistance is the resistance of the electrolyte, electrodes, and leads to the applied voltage. It is defined by Ohm's law viz.

$$i_s = -\boldsymbol{\sigma}_s \nabla \phi_s \text{ with current conserved } \nabla i_s = Q_s$$

where i_s = current density vector in A m^{-2}

$\boldsymbol{\sigma}_s$ = conductivity in S m^{-1}

ϕ_s = electric potential of the metallic conductor in V

Q_s = current source term in A m^{-3}

In terms of the Nernst-Planck equation we assume the equation to have zero velocity, uniform carrier ion concentration, and non - uniform conductivity. A post solution current density term J can be added to define molar flux.

$$\partial c/\partial t = 0 = \nabla \cdot [\, (D\ z\ e / k\ T)\ c\ \nabla\Phi]$$

The field variables are electric potential Φ and carrier concentration c. We assume the carrier concentration to be uniform therefore reducing the equation to

$$\nabla\cdot (\sigma\ \nabla\Phi) = 0$$

Adding a current density term J to the solution gives us,

$$J = -\sigma\ \nabla\Phi$$

which is Ohm’s law in the potential form.

3.1.3 Secondary Current Density Distribution

The secondary current density distribution is defined as the combination of ohmic resistance and activation overpotential. The activation overpotential is the activation energy needed for the charge transfer reaction in the system. The electrode kinetics (charge transfer) is an important factor in the modelling of electrolysis as it determines rate of the reaction. The secondary current density can be formulated as the Nernst-Planck equation with a velocity term added to the equation and steady state ionic concentration (i.e., this term can be assumed to be zero). The charge transfer which is the relation between the electrode and electrolyte interface can be modelled using the Butler-Volmer equation or the Tafel equation.

The Butler-Volmer equation is given by,

$$i_{loc,\,m} = i_{0,\,m}\,(\exp\,((\alpha_a\,F\eta) / R * T) - \exp\,((-\,\alpha_c\,F\eta) / R * T))$$

where $i_{0,\,m}$ = exchange current density in A m^{-2}

α_a = anodic charge transfer coefficient

α_c = cathodic charge transfer coefficient

The transfer coefficient of both anode and cathode are assumed to be symmetric at both electrodes and therefore $\alpha = 0.5$.

3.1.4 Tertiary Current Density Distribution

The tertiary current density is a combination of the ohmic resistance (primary distribution), activation overpotential (secondary distribution) and the concentration overpotential. The change in concentration changes the electrolyte composition and the ionic concentration of the electrolyte. All three terms in the Nernst-Planck equation of diffusion, migration and convention are modelled in the tertiary current density.

Mathematically the tertiary current density is described as

$$i_{loc,m} = i_{0,m} \left(\left(C_{red} / C_{ref} \right) \exp \left((\alpha_{a,m} F\eta_m) / R * T \right) - \left(C_{Ox} / C_{ref} \right) \exp \left((- \alpha_{c,m} F\eta_m) / R * T \right) \right)$$

C_{red} = concentration of the species to be reduced

C_{Ox} = concentration of the species to be oxidised

The tertiary current density solves the Nernst-Planck equation using explicit time stepping for every species in the solution to describe mass transport through all three parameters of diffusion, migration, and convection. The electrochemical reactions' kinetic expressions account for both activation and concentration overpotentials, signifying that the electrolysis reaction rate can be limited by reactant depletion at the electrode-electrolyte interface. Consequently, the model must incorporate all ions and electroactive species present in the electrolyte.

3.2 MHD

In this section the concepts of how electromagnetic flow happens is explained with respect to molten salts. Also, the essential equations and model dimensions are described.

3.2.1 Electromagnetic Induction Due to Busbars and Current Flow

A current carrying conductor creates a magnetic field around it and this magnetic field interacts with any charged matter or magnetic fields present to produce a force. These induced magnetic fields interact with the ionically charged molten salt in an electrochemical cell to cause flow of the electrolyte. The flow rate of molten salt depends on the electrical conductivity of the salt. The fluid flow can also induce a change in the potential difference. This phenomenon is important to prevent rate limiting kinetics and also improve busbar design in large scale cells. The magnetohydrodynamic problem is solved by modelling the Navier-Stokes equations and Maxwell's equations and coupling them.

This interaction of a magnetic field and electrical current induces forces in the system called Lorentz forces which can accelerate the fluid flow. This can change the boundary layers around the electrodes and affect other macroscopic effects in the cell such as heat transfer, and current density.

3.2.2 Modelling of Electrolyte Flow

The electrolyte flow in the system is governed by the conservation of mass, momentum and energy as standard in continuum mechanics. The following equations describe all three important parameters for the molten salt electrolyte in the system.

Conservation of mass is given by,

$$(\partial \rho / \partial t) + \nabla (\rho V) = 0$$

where ρ is the density with unit mass per unit volume.
This equation is known as the *continuity equation*.

Conservation of energy is given by,

$$((\partial \rho\ C_p\ T) / \partial t) + \nabla . (\rho\ C_p\ T\ V) = \nabla .\ k\ \nabla\ T + H$$

where the amount of heat per unit volume is given by ρCpT where C_p is the specific heat at a constant pressure and T is the temperature. k is the thermal conductivity of the of the system and $\rho CpTV$ is the transport flux of the system. H is the heat source term.

Conservation of momentum is given by

$$(\partial \rho V / \partial t) + \nabla (\rho V V) = \nabla \sigma + \rho g$$

where ρV is the momentum per unit volume, g is the net acceleration.

Here, in addition to gravitational acceleration, the system encounters a Lorentz force F.

Molten salts, especially fluorides are considered to have high viscosity and therefore we have considered only laminar flow of an incompressible fluid while modelling this system. The temperature of the salt is assumed to be constant within the region of flow with constant electrical conductivity and pressure. Considering a steady state flow problem, we can reformulate the equations mentioned above as

$$\nabla . V = 0 \text{ (mass conservation)}$$

$$\nabla . (\rho C_p T V) = \nabla. (k \nabla T) \text{ (energy conservation)}$$

$$\nabla (\rho V V) = \nabla \sigma + \rho F \text{ (momentum conservation)}$$

To further simplify the problem, we assume strong viscous laminar flow leading to a small Reynold's number i.e., the ratio of inertial acceleration in the fluid to the viscous force.

$$R_e = (V_0\ L) / v$$

The Reynold’s number also controls the width of the boundary layer in the problem formulation.

The currents induced in the system due to fluid flow gives rise to Lorentz forces as mentioned above and alters the velocity profile. Due to the external magnetic field and currents generated in the fluid, there are additional magnetic fields generated in the fluid.

Considering the external magnetic field due to flow of current in the busbars, the magnetic field of the fluid is

$$B = B_o + b$$

Applying this condition to the conservation equations we get

$$\nabla \cdot V=0$$

$$(\partial \rho V/\partial t) + \nabla(\rho VV) = \nabla\sigma + \rho\ (J \times B)$$

$$((\partial \rho\ C_p\ T) / \partial t) + \nabla \cdot (\rho\ C_p\ T\ V) = \nabla \cdot (k\ \nabla\ T) + (J^2/\sigma)$$

where $(J \times B)$ is the Lorentz force term and (J^2/σ) is the Joule heating term.

To determine the magnetic field (B) and electric charge (J) we use Maxwell’s equations in potential form. Maxwell’s equations are represented in terms of electric and magnetic fields but can also be expressed in terms of electric potential φ, and magnetic potential, A.

$$\nabla^2 A - \mu^0 \epsilon^0 (\partial^2 A / \partial t^2) = -\mu^0 J + \nabla (\nabla \cdot A + \mu^0 \epsilon^0 (\partial \varphi / \partial t))$$

$$\nabla^2 \cdot \varphi + \partial / \partial t (\nabla \cdot A) = -\rho / \epsilon_0$$

The Maxwell’s equations combined with current density gives us

$$J = \sigma (E + V \times B),\ F = J \times B$$

3.3 COMSOL Finite Element Model

The goal of the finite element model is to determine the characteristics of the cell based on applied voltage, and current flowing through the system. The current density distribution also varies with different cathode thicknesses and estimation of current density and total current determines optimal growth conditions. The simulations carried out in COMSOL Multiphysics use the electrochemistry, AC/DC, transport of diluted species and laminar flow modules. The COMSOL versions used were 5.5, 5.6 and 6.0. COMSOL has downwards compatibility and therefore newer model versions can be run on older versions. The geometry of the cell was defined and assembled in Solidworks and imported into COMSOL using the CAD module. It was rebuilt in COMSOL using the COMSOL kernel. Property definitions, materials properties and definitions, boundary conditions and equations were coupled in the software before mesh parameters were chosen. After meshing the simulation was solved in the study step where solver parameters can be input. Post processing was done in the same software and the solution need not be exported for post processing.

The modelling workflow consisted of the following steps,

- Setting up the modelling environment
- Building the geometry
- Specifying material properties
- Defining boundary conditions
- Creating the mesh
- Running the simulation
- Post Processing

3.3.1 Meshing

Meshing is important in finite element analysis. An accurate mesh is essential for accurate results. Meshing needs a balance between size of the mesh and solution time. Coarser meshes give quicker results but can have inaccuracies whereas as meshes become finer the solution time increases proportionally but can lead to more accurate results. A grid independence test can be performed to determine if the solution is sufficiently converged, and the results are acceptable. This test ensures the accuracy of the problem.

A grid independence test is done by choosing a mesh initially and then refining that said mesh to the next coarser mesh size and then next finer mesh size. A steady solution is said to be reached when the mesh refinement produces minimal change in the solution. Factors such as number of elements, size of each element, and grid size affect this result.

3.3.2 Cell Geometry

The design of the cell considered for modelling is based on an aluminium potline of the Hall-Héroult process. The manufacturing plant would consist of multiple cells each with its own DC rectifier and busbar as shown in the figure below.

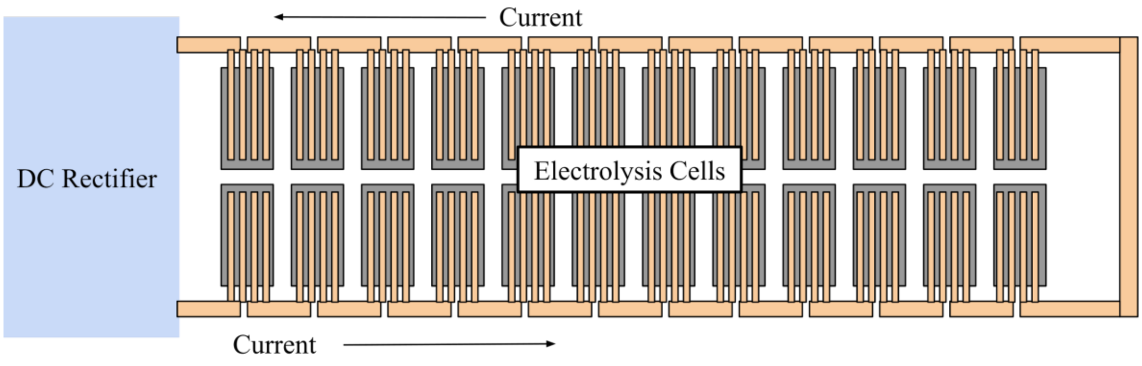

Figure 4: Top view of a silicon potline

The optimal operational temperature range of the process is between 980^0C and 1200^0C. The lower limit is due to the eutectic temperature of the CaF_2 - MgF_2 mixture and the upper limit is due to factors such as volatility, material constraints, and cell design. Higher temperatures would lead to higher conductivities of the silicon, molten salt, and zirconia which would improve energy efficiency. But these temperatures could also lead to material degradation and the inclusion of impurities in the system. The model in this study has a temperature of 1100^0C.

Two design parameters for the cathodes can be considered based on form factor viz. slab or cylindrical cathodes. The advantage of a cylindrical cathode is that they can be rotated to stir the bath and promote mass transfer and prevent rate limiting kinetics. But this may cause uneven growth and change the surface area of the cathode as there is growth of silicon product. The other consideration is of slab cathodes. Slab cathodes have the advantage of having a compact form factor and a large surface area. But due to this, they might have some rate limiting factors preventing easy movement of electrolyte and silicon product could unevenly deposit at the edges of the cathode. This can be avoided by moving the cathode side to side but would require appropriate design engineering.

For the modelling of the cell, we consider a single cell in a potline with a 300 kA bus. In terms of dimensions, a Hall-Heroult aluminium cell with 1 A cm^{-2} anode current density could have one or more anodes with a footprint totalling 1.4 × 7.1 m = 9.94 m^2. The cathode density current is in the range of 0.6 - 0.8 A cm^{-2} in the cell. The cell and busbar arrangement shown above in Figure 4 is assumed to produce a vertical magnetic field.

3.3.3 Anode Design

The anode used in the model is a thick porous electronically conductive membrane coated on the inside of a yttria stabilised zirconia (YSZ) vertical tube closed at one end. The YSZ tube is a porous solid electrolyte which selectively diffuses oxygen through the membrane which then comes in contact with the anode material giving rise to pure oxygen. The anode material can be a noble element such as silver or a thin rare earth nickelate like LSM or LCS as mentioned in chapter 2 and (< 1 mm) also seen in solid oxide fuel cells. The solid oxide electrolyte can be YSZ, scandia stabilised zirconia (ScZ), samaria or gadolinia doped ceria as mentioned in chapter 2.

In the cell modelled, the SOM tubes have a 3 cm outer diameter with 52 cm of immersed length without the hemispherical end. This leads to a surface area of 504 cm^2 of the SOM - bath interface. There is no gas evolution in the melt like an aluminium cell and therefore there is no gas lift stirring of the melt. Therefore, due to this design, MHD is likely the best stirring mechanism to promote kinetics as mentioned.

3.3.4 Slab Cathodes

The design for slab cathodes is shown in the figure 5 below. The slab cathodes as mentioned before have a smaller form factor in terms of the cell and can be easily changed out rather than cylindrical cathodes. They can also be easier to post-process when the silicon needs to be sliced into wafers.

The figure shows cathodes arranged parallel to each other all along the cell with the anodes between the cathodes and the ends of the cell. Anodes are 13.5 cm from in between the slab centre in both directions providing an equal 10 cm of space anode-cathode distance. Each cathode has a minimum thickness of 4 cm and a length of 2.5 m and depth of 1.2 m. Each cathode has a surface of 3 m^2 on each side and total surface area of 6 m^2 considering both sides are exposed to the flux. Each cathode has 15 kA of current with 0.25 A cm^{-2}.

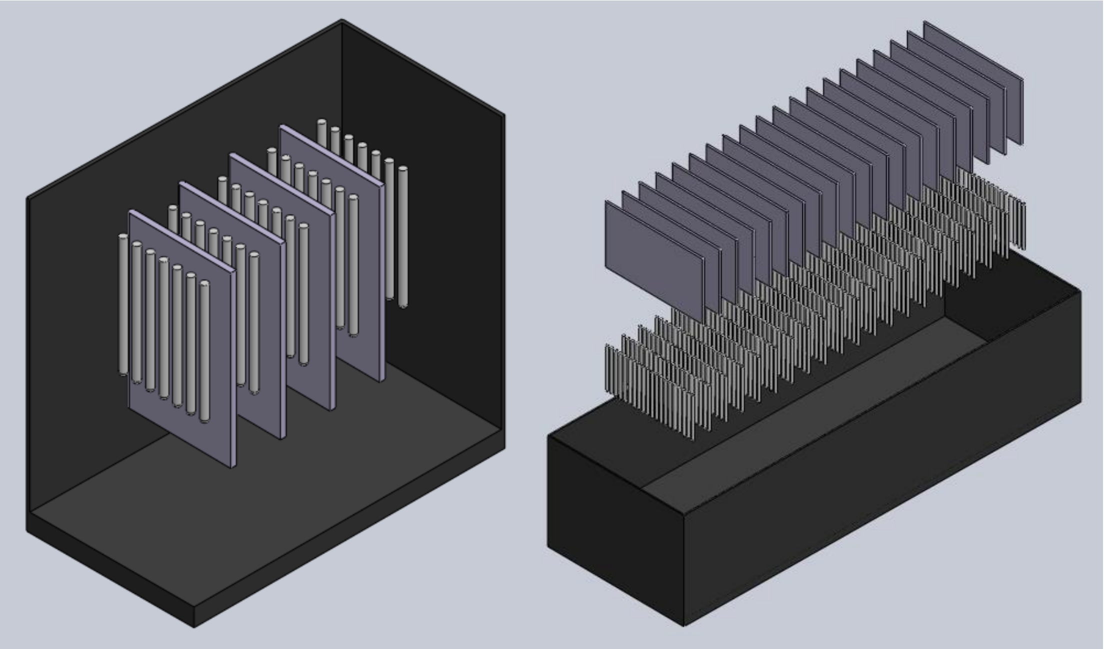

Figure 5: Expanded view of slab cathodes and cylindrical anodes

3.3.5 Primary Current Density

The geometrical configuration employed for the model encompasses one-quarter of the solid oxide membrane (SOM) anode and half the thickness of the cathode, as depicted in the accompanying figure. This representation constitutes the minimal primitive unit cell of the large-scale system, exhibiting a current density distribution analogous to the entirety of the anode and the majority of the cathode surfaces, excluding peripheral regions. For the purposes of this simulation, the anode is postulated to consist of commercially pure nickel, featuring a current collector of analogous composition. The anode thickness is assumed to be equivalent to the SOM, measuring 2 mm.

The electrodes are submerged in a molten salt bath, with a composition of CaF_2 - MgF_2 - CaO - Y_2O_3 - SiO_2 having a temperature dependent conductivity of 438 S m^{-1}

at 1100^{0}C as determined by Villalón et al. 2018. The material properties for the SOM conductivity, nickel conductivity was taken from (Cezairliyan & Miiller, 1983; Krishnan, 2006; Wouters et al., 1976) .

As shown in the graph below, nickel and silicon have much higher conductivities compared to the liquid and solid electrolyte (SOM) and therefore we can assume that the cell resistance is low. The electrolyte density is estimated based on the temperature-dependent molar volumes of CaF_2 - MgF_2 which are its main constituents.

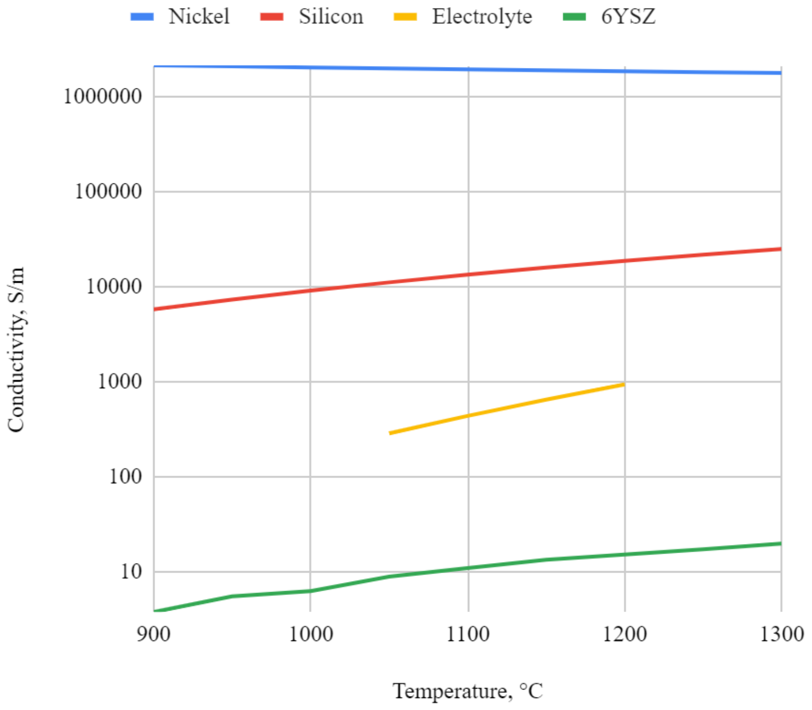

Figure 6: Temperature dependent conductivity of cell materials.

The COMSOL electrochemistry module (add-on module) is used to construct the finite element model and also define the boundary conditions for the primary current density distribution. The model is broken down into the smallest primitive unit of the cell viz. One quarter of the cathode and half the anode as shown in Figure 7. The initial mesh used is a “fine” free-size tetrahedral mesh, defined by COMSOL’s physics-based automatic meshing option. The maximum mesh element size is 0.09 m, and the minimum mesh element size is 0.0162 m for all three models. The total number of elements is approximately 63,000 elements encompassing domain, boundary, and edge elements.

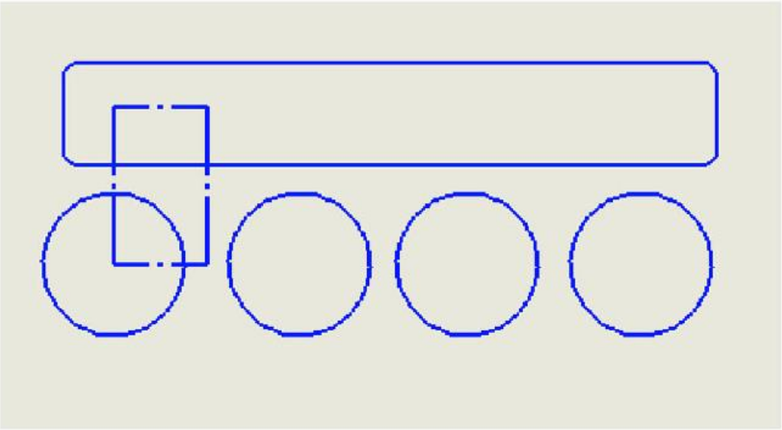

Figure 7: Smallest primitive unit of the cell represented by one quarter anode and half the cathode.

A grid independence study was conducted by reducing the mesh size to a maximum mesh element size of 0.0495 m and a minimum mesh element size of 0.0046 m, with a curvature factor of 0.4, using the “finer” physics based meshing option available in COMSOL.

3.3.6 Secondary Current Density and Tertiary Current Density

A similar geometry was used for the secondary current density as described in the primary current density. We add the transport of diluted species node to simulate the electromigration of the species in the electrolyte due to the electric field. We assume very fast reaction kinetics and diffusion kinetics for the system between the electrode - electrolyte interface. The equations used are

$$\nabla \cdot J_i + u \cdot \nabla c_j = R_i$$

$$J_i = - D_i \nabla c_i - z_i u_{m,i} F c_i \nabla V$$

The tertiary current density is simulated by retaining the conditions of both primary and secondary current density and adding the laminar flow node to the model. The tertiary current density as mentioned considers the flow of the species in the cell thus changing concentration gradients and the current density.

3.3.7 MHD Implementation

The MHD is implemented using the AC/DC module and fluid flow module and coupling it with the current density computed in the previous step. The direction of flow is determined by the right-hand rule and inlet and outlet boundary conditions are defined in the geometry based on this. The diffusivity is calculated using the Nernst-Einstein relation shown below.

$$\Lambda_m^0 = (F^2 / R T) (v_+ z_+^2 D_+ + v_- z_-^2 D_-)$$

where v_+ and v_- are the number of cations and anions per formula unit of electrolyte, z_+ and z_- are the valencies of the ions and, D_+ and D_- are the diffusion coefficients of the ions.

A normal velocity boundary condition is applied at the inlet of the model based on the right-hand rule. The walls have a no-slip boundary condition with the outlet set to be a pressure condition with p = 0 with no backflow. The Lorentz force is implemented using the volume force condition which is coupled with the fluid velocity field.

The fluid domain is governed by Ampere's law and current conservation principles to capture the properties of both magnetic and electric fields. The computational region is modelled like a flow metre and is subjected to Ampere's law, and its boundary is magnetically insulated. The MHD was modelled based on the example by (*Building a Magnetohydrodynamic Multiphysics Model in COMSOL® | COMSOL Blog*, n.d.)

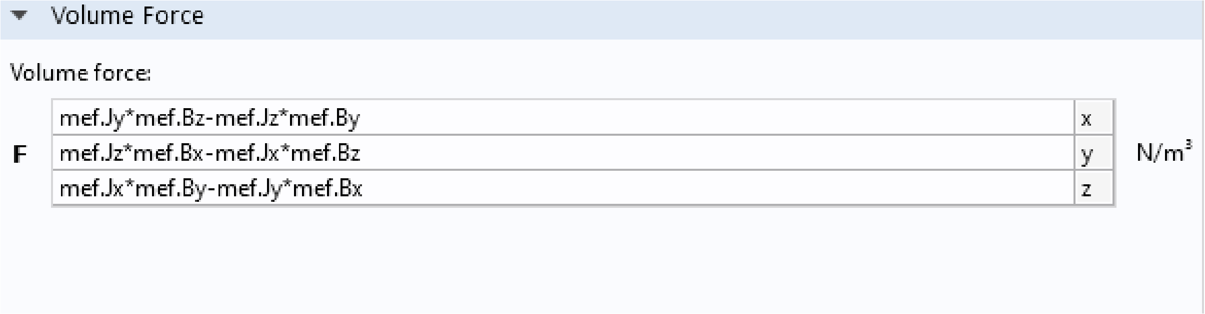

mef.Jy*mef.Bz-mef.Jz*mef.By
mef.Jz*mef.Bx-mef.Jx*mef.Bz
mef.Jx*mef.By-mef.Jy*mef.Bx

Figure 8: COMSOL window showing the coupling of the volume force in MHD.

3.4 Results and Discussion

3.4.1 Primary Current Density

The figure 9 below illustrates the computed primary current density distribution, represented as current streamlines, for four distinct cathode slab thicknesses ranging from 2 cm to 8 cm (corresponding to half-thicknesses of 1 cm to 4 cm). The current density appears to be relatively uniform across the anode - SOM interface, and for most of the cathode at increased thicknesses, although current concentration is observed at the cathode's lower extremity. Figure 9 also presents the electrical potential distribution throughout the model domain.

The model computes the current for one-quarter of an anode. Therefore, multiplying by four yields the total anode current, while dividing the model output by the cathode area within the model (360 cm²) provides the average cathode current density. The table 2 below displays the total current per anode and the average current density on the cathode surface as a function of cathode thickness.

Cathode thickness (cm)	**Anode current (A)**	**Average cathode current density (A/cm^2)**
2.0	95.9	0.066
4.0	133.0	0.092
6.0	156.0	0.108
8.0	173.8	0.121

Table 2: Calculated cell current per anode and average current density at cathode – electrolyte interface

For a cathode thickness of 4.0 cm, the anode current calculated utilising COMSOL's "finer" mesh option is 1.3% lower than the result obtained using the "fine" option, which is employed for most of the solutions.

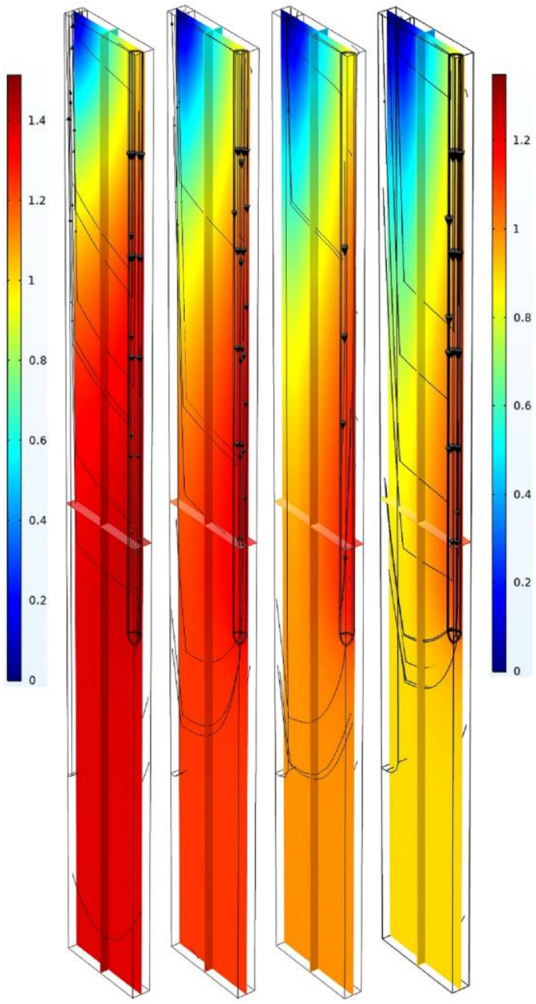

Figure 9: Primary current density and electrical potential distribution for cathode thicknesses of 2 cm, 4 cm, 6 cm, and 8 cm (Half thicknesses: 1 cm, 2 cm, 3 cm, 4 cm in the model)

3.4.2 Secondary and Tertiary Current Density Distribution

The secondary and tertiary current density are illustrated below for two different geometries. The models show that there is very slow migration and flow of ions in the system. The current density is uniform along the surface but concentrated at the edges of the SOM tube.

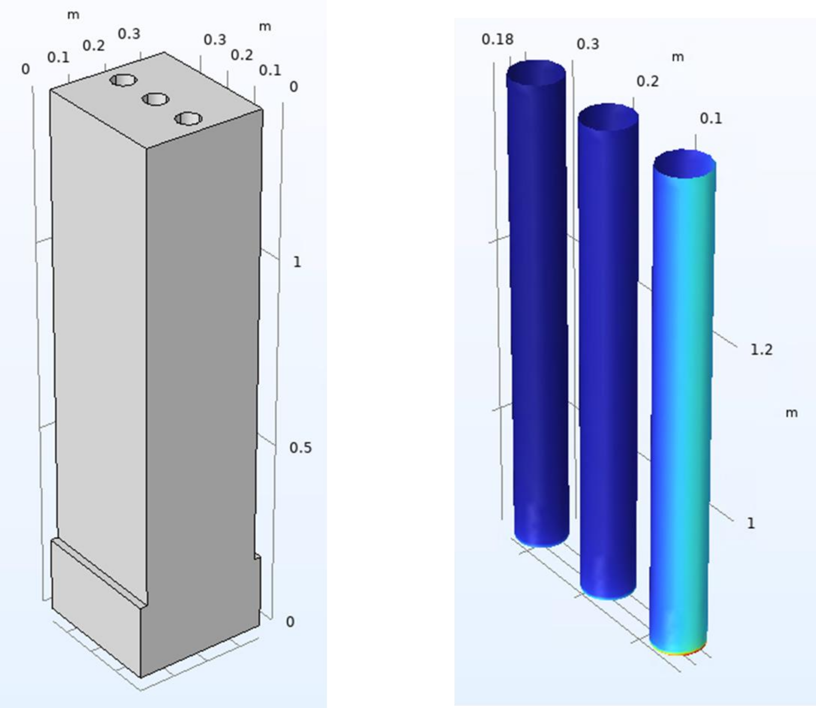

Figure 10: Tertiary current density for geometry shown in the figure on the left

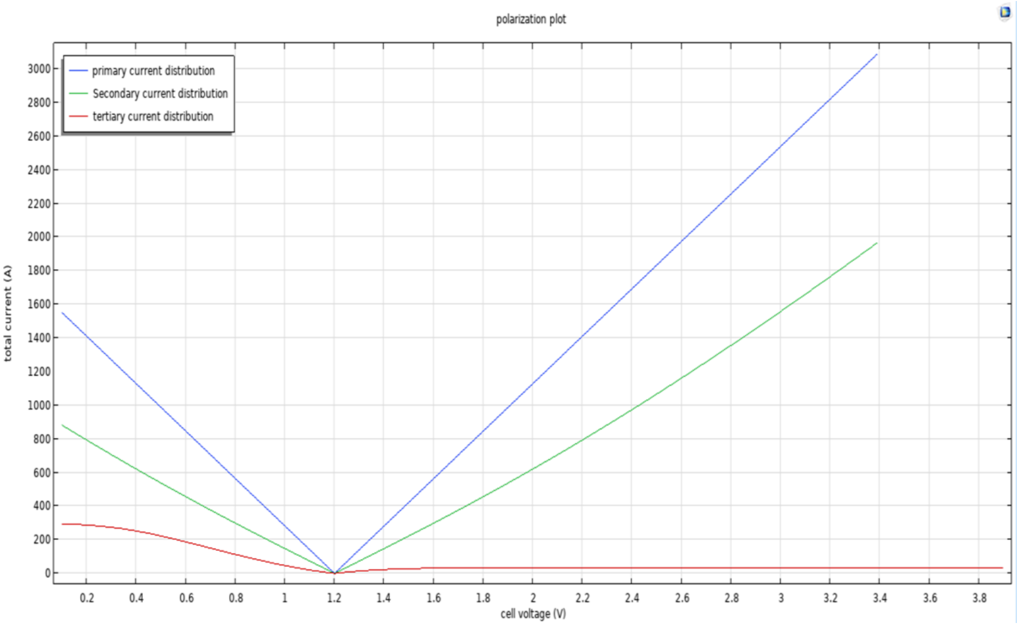

Figure 11: Polarisation plots for primary, secondary, and tertiary current density distribution

3.4.3 Magnetohydrodynamics

A solution to the Lorentz force was analytically calculated and was compared to the COMSOL model. The analytical solution calculated found the ionic velocity to be six orders of magnitude higher than the value calculated in the COMSOL model. To analytically calculate the value of the Lorentz force we first calculate the magnetic field strength. The current density from the primary distribution is 0.5 A cm^{-2}.

To calculate the magnetic field strength for a current density of 0.5 A cm^{-2}, 1 m from the conductor, and the conductor being in the electrolyte, we can use the formula:

$$B = (\mu_0 * I) / 2 \pi r$$

where B is the magnetic field strength, I is the current through the entire cell (300 kA), r is the distance from the conductor, and μ_0 is the magnetic constant of free space. We have $r = 2.7$ m, and $\mu_0 = 4\pi \times 10^{-7}$ T m A^{-1}.

Substituting these values in the formula, we get:

$$B = (4\pi \times 10^{-7} \text{ T m A}^{-1}) \times (300{,}000 \text{ A}) / 2 * \pi * 2.7 \text{ m}$$

$$B = 0.0223 \text{ T (tesla)}$$

The magnetic field from the conductor from the opposite side is at 8.1 m away giving us a field strength of $7.41 * 10^{-3}$ T for a total field strength of 0.0291 T.

Therefore, the total magnetic field strength for these given parameters is approximately 0.0291T tesla.

Using the values of the magnetic field strength calculated and the electric current density of 0.5 A cm^{-2}, the Lorentz force can be calculated as

$$F = J \times B$$

where B = 0.0291 T and J = 0.5 A cm^{-2}

Substituting these values in the above formula, we get:

$$F = (0.0291\ T) \times (5000\ A\ m^{-2})$$

$$F = 145.5\ N\ m^{-3}$$

Therefore, the Lorentz force on the conductor is approximately 145.5 N m^{-3}.

To calculate the speed of a silicon ion in response to the Lorentz force of 145.5 Nm^{-3}, we need to know the charge and mass of the ion. The charge of a silicon ion is +4, where e is the elementary charge, which has a value of approximately 1.602×10^{-19} coulombs (C).

The mass of a silicon ion is approximately 28 atomic mass units (amu) or 4.65×10^{-26} kg. Using these values, we can calculate the speed of the silicon ion as follows:

$$v = F / (q \times B)$$

where F is the Lorentz force of 400 N, q is the charge of the silicon ion +4, and B is the magnetic field strength of 0.02 tesla.

Substituting these values in the above equation, we get:

$$v = (145.5 \text{ N m}^{-3}) / ((+4) \times (0.0291 \text{ T}))$$

$$v = 1250 \text{ m s}^{-1}$$

Therefore, the estimated velocity of a silicon ion in response to the given Lorentz force is approximately 1250 m s^{-1}

The highest velocity seen in the COMSOL model is near the anode of the cell which is on the mm scale.

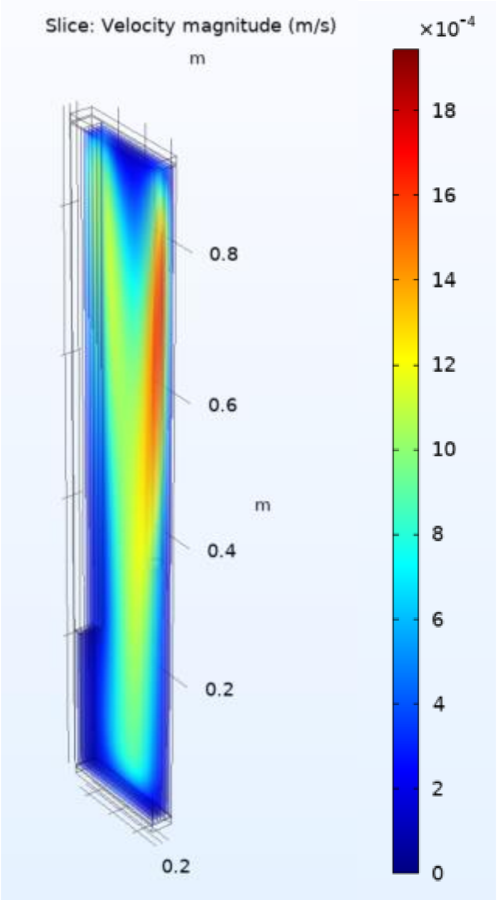

Figure 12: MHD COMSOL model showing slow rate of flow of electrolyte.

Chapter 4 - Experiments

This chapter describes experimental work carried out using a solid silicon cathode and the molten salt composition of a CaF_2 - MgF_2 eutectic with CaO as a solvating agent, Y_2O_3 (in place of YF_3) for membrane stability and SiO_2 (Villalon, 2018).

4.1 Experimental cell

The electrolytic cell used in the electrolysis is shown in Figure 13 below. The outer tube inside the furnace is made from 310 stainless steel and this is chosen due to good corrosion resistance and heat resistance at high temperatures. The inside cage has three baffle plates of 304 stainless steel. The baffles act as an effective heat containment mechanism reflecting heat back and protecting the top flange of the setup. The entire setup is enclosed in a Mellen furnace with a maximum temperature rating of 1200^0C.

The setup was initially purged using argon providing an inert environment and also prevented the formation of oxides which would cause corrosion. Subsequently, forming gas with 2.93% hydrogen in argon was used to prevent even trace amounts of oxygen in the system.

Figure 13: a. Setup of cage inside the furnace (left). b. The image on the right showing mechanical method of holding silicon wafer with YSZ membrane (right)

4.1.1 Solid Cathode

A solid cathode can be used to electrowin silicon in the SOM process. It has been previously shown that molybdenum can be used, but the silicon has been deposited in the form of $MoSi_2$. Considering this it was decided to use pure silicon as a cathode. Silicon can be a good ionic conductor and stable to prevent salt entrapment in the interface. A sufficiently thick piece of wafer or a coated wafer will not react with oxygen or oxide ions in the melt. The high density of 2.3016 g cc^{-1} at 1027^0C also prevents deformation and creep effects in silicon. Using silicon also promotes nucleation and growth due to affinity of ions in the melt, to the cathode. All these criteria make silicon a suitable solid cathode.

4.1.2 SOM anode

The anode of the system was enclosed by a hollow solid electrolyte, 1.8 cm in diameter. The solid electrolyte was an yttria stabilised zirconia membrane with a hemispherical end and open at the other end. Liquid silver was used as an anode, and this is due to silver’s ability to not oxidise at high temperatures and promote movement of oxygen ions. A graphite current collector was used. Though the use of a graphite as a current collector produces CO_x, the ability to quickly iterate and turnaround experiments made it an attractive option. The cell showed low resistivity due to using graphite as an anodic current collector. The graphite current collectors needed to be sanded down to appropriate diameters to fit into the membrane. The cell resistance was also very low due to the use of the graphite current collector.

4.1.3 Crucible design

The crucible initially used was a graphite crucible following the same principle of ease of use and quick proof of concept. The graphite crucibles used were found to contaminate the flux forming silicon carbide as analysed by energy dispersive x-ray spectroscopy (EDS) and therefore a stainless-steel crucible was used. Due to the operating temperature of the system and the nature of the fused salt, there were very small trace amounts of cobalt and a large amount of iron in the flux after electrolysis during use of the steel crucible. Therefore, to prevent this contamination, a stainless-steel crucible sprayed with boron nitride was used.

4.2 Experimental Procedure

The experimental procedure involved two major steps i.e., salt preparation and electrolysis. Preparation of salts is an important step to prevent the contents of the salt from reacting with atmospheric oxygen leading to absorption of moisture. Also, due to the relatively high temperature these experiments are run at and the reactive nature of these salts, pre-treatment of the salt prevents corrosion with the internal structure of the stainless-steel tube.

Firstly, the CaF_2 - MgF_2 eutectic with the CaO and Y_2O_3 was individually dried out to remove adsorbed water. The initial weights of the salts changed after this operation. These four salts, the fluorides and the oxides are then combined in their respective ratios, mixed mechanically and pre-melted in the setup under an inert environment. The initial ratio of the salts was taken from (Villalon et. al., 2018) viz. Calcium fluoride being 48.86 wt.%, magnesium fluoride being 36.41 wt.%, calcium oxide being 6.69 wt.%, and yttrium oxide being 3.10 wt.%. The original composition used yttrium fluoride (YF_3) but was substituted with yttrium oxide (Y_2O_3) due to its lower yttrium-basis cost. This required changing the weight fractions of the remaining components to keep the silicon oxygen ratio like that previously engineered, which is 4 mol: 1 mol. The resulting salt mixture was then crushed, and 5 wt.% silicon oxide was added to this mixture. This mixture with the crushed salt and powdered silica was then immediately used for electrolysis.

Initial furnace tests determined a furnace temperature profile, and this helped in determining the optimal heat zone to place the crucible in. A major challenge involved determining a method to hold the silicon wafer to the stainless-steel current collector. Both mechanical and chemical methods were explored. A slit based on the thickness of the wafer was cut in the current collector using an electric discharge machine (EDM). The silicon wafer was inserted in this slit and was held in place using a high temperature stainless steel conductive adhesive from the Cotronics Corp. (Durabond 954 series adhesive). The stainless-steel adhesive needed 24 hours to cure at room temperature and needed further curing between 200^0C and 300^0C post the 24 hours for 2 ~ 3 hours. A second mechanical method to hold the wafer was to drill and tap a ¼ inch hole through the current collector and use ¼ - 18-inch screws to hold the silicon wafer in place.

The SOM cell was heated to 1100^0C in a ramp-hold program in steps to remove all moisture from the salts and not subject the YSZ membrane to thermal stresses due to a fast ramp rate. Once the furnace reached temperature, it was allowed to equilibrate till the inside temperatures reached the desired value of ~1100^0C. Once the set temperature was achieved, the electrodes were lowered into the melt for electrolysis. Post electrolysis the electrodes were raised from the flux and the furnace was let to reach room temperature. The cell was maintained in an inert environment throughout the experiment.

4.3 Electrolysis and Electrochemical Characterisation

Pre - Electrolysis, a potentiodynamic scan was performed across the electrodes to determine the dissociation potential of silicon dioxide in the system.

The potentiodynamic scans were performed using an Agilent 6033A auto ranging system DC power supply. The voltage was increased from 0 V to 5 V in steps of 0.1 V every 10 s. This gave us a scan rate of 100 mV s^{-1}. Since the initial tests were done using a graphite crucible and then a stainless-steel crucible, to mitigate impurities in the system, a pre-electrolysis potentiostatic hold was applied at 1.5V for 1 hour. Post this, the power supply was switched off and the system was allowed to equilibrate for ~10 minutes.

An Electrolysis hold was then applied for varying durations in the experiments before the system was switched off and allowed to equilibrate. This procedure of a sweep and a hold was repeated multiple times depending on the amount of flux in the system. Post electrolysis the furnace was allowed to cool down before characterisation of the sample.

The silicon cathode was separated from the steel current collector and characterised using a JEOL JSM-7000F scanning electron microscope with an Oxford instruments EDS system. The initial experiment samples were hot mounted in epoxy and polished, but it was seen that hot mounting caused the wafer to break. Subsequent samples were all cold mounted before polishing and characterisation.

Following the above procedures, multiple experiments were carried out. The major initial challenge faced was that of the cathode thinning in size and this was attributed to not having an oxygen free inert environment. The initial wafers used were uncoated 625 µm pure silicon wafers from the company University Wafers. The mechanism of thinning is suspected to be due to the reaction shown below in the melt.

$$SiO_2 + 2O^{2-} \rightarrow SiO_4^{4-}$$

One way to mitigate this was to bury the wafer into the melt and perform electrolysis. The second method explored was using a silicon nitride (Si_3N_4) coated silicon wafer of 525 µm with a 300 µm coating. It was finally decided to switch to a thicker 1065 µm wafer to prevent thinning and keep the wafer mechanically stable to avoid creep.

Another initial challenge was the breaking of the YSZ tube and loss of silver into the flux. This was due to rapid insertion of the tube into the melt at the electrolysis temperature causing thermal shocks to the tube. This was mitigated by starting with the tube at the depth required for electrolysis and ramping up the furnace at a slower ramp rate of 2^0C ~ 5^0C.

A typical ramp - hold profile is shown in the table 3 below.

Temp (^{0}C)	Ramp Time (min)	Hold Time (min)
0 → 350	175	180
350 → 550	100	150
550 → 850	150	150
850 →1050	100	120
1050 →1130	40	Completion of Electrolysis
1130 → 30	22	15

Table 3: Ramp – Hold furnace profile

To calculate the thickness of the deposit Faraday's law of electrolysis was used assuming Faradaic efficiency. The mass of the deposit is calculated by,

$$m = (Q * \eta * M) / (n * F)$$

where Q = amount of charge passed through the cell in coulombs

η = Faradaic efficiency of the deposition process

M = Molar mass in g mol^{-1}

N = number of electrons transferred during the deposition reaction

F = Faraday's constant viz. 96485 C mol^{-1}

From this mass the volume of the deposit is given by

$$V = m / \rho$$

ρ = density of material which is 2.33 g cm^{-3}

And to find the thickness (t) of the deposit, the volume is divided by the area,

$$t = V / A$$

A = area of electrode where the deposition is taking place in sq. * m

To calculate the time of electrolysis knowing the mass of the product in the flux, the molar mass (M) of the product was determined in grams per mol (g mol^{-1}). The number of moles (n = m/M) was calculated, and the number of electrons (z) involved in the reaction per mole of product was determined. Here silicon has 4 electrons that take place in the reaction. Subsequently the total charge using Faraday's constant, the current density (j) in Amperes per square metre (A m^{-2}) and total current was calculated.

$$Q = n * z * F \text{ where } F = 96485 \text{ C mol}^{-1}$$

$$I = j * A$$

Multiplying the current with the Faradaic efficiency η would give us the effective current I_{eff} which when used to divide the charge would give us time in seconds.

$$I_{eff} = I * \eta$$

$$t\ (s) = Q / I_{eff}$$

Experiment 7 showed a dissociation potential of 1.8 V from the potentiodynamic scan shown on page 11. Based on this electrolysis was done at 2V for 30 minutes. The post experimental characterisation showed a deposit of ~ 2 - 3 µm. But the theoretical thickness calculated by assuming Faradaic efficiency was 296 µm. It was hypothesised that running an experiment at a higher voltage therefore driving more current into the system and for a longer duration would give us a thicker deposit.

Based on the assumption that higher voltage would drive more current through the system Experiment 8 was run at 3.7 V. But, in the post characterisation of the sample it was seen that the flux was contaminated with carbon and there was thinning of the wafer.

Experiment	Initial Condition	Result
1	Original flux composition with solid cathode	Low current, 0.01 - 0.02 A
2	Original flux composition with solid cathode	Low ohmic current, YSZ tube broke during electrolysis
3	Original flux composition with solid cathode	Low current, cathode thinning observed
4	Original flux composition with solid cathode	No current measurement
5	Original flux composition with solid cathode	YSZ tube broke during insertion
6	Original flux composition with solid cathode	No current measurement
7	Original flux composition with solid cathode. Voltage above dissociation potential	First successful run, no measurement of current after second hold
8	Original flux composition with solid cathode. High voltage	Thinning of wafer was observed but salt adhered to wafer. Formation of SiC.
9	Original flux composition with solid cathode	Switched to a stainless crucible. Long electrolysis run at a higher voltage. Wafer lost in salt.
10	Original flux composition with solid cathode	Stainless crucible. Long electrolysis run. Iron leached into the system

Table 4: Experimental summary of initial ten experiments

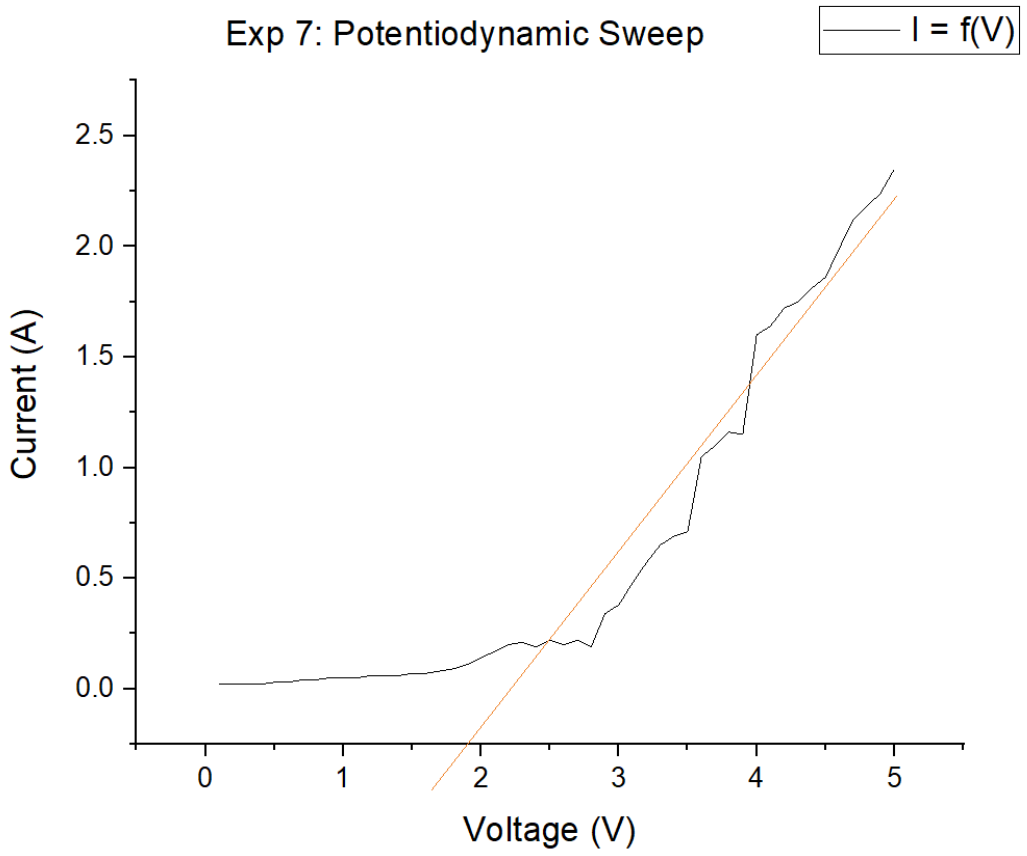

Figure 14: Potentiodynamic scan pre-electrolysis showing dissociation potential to be 1.8 V.

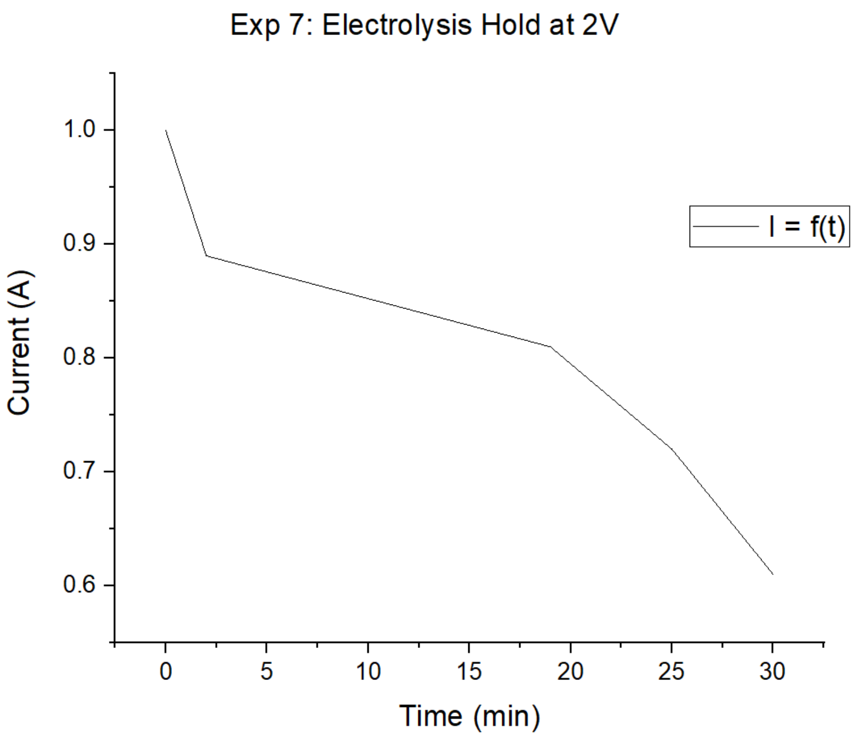

Figure 15: Current as a function of deposition time. Area under the curve indicates the amount of material deposited.

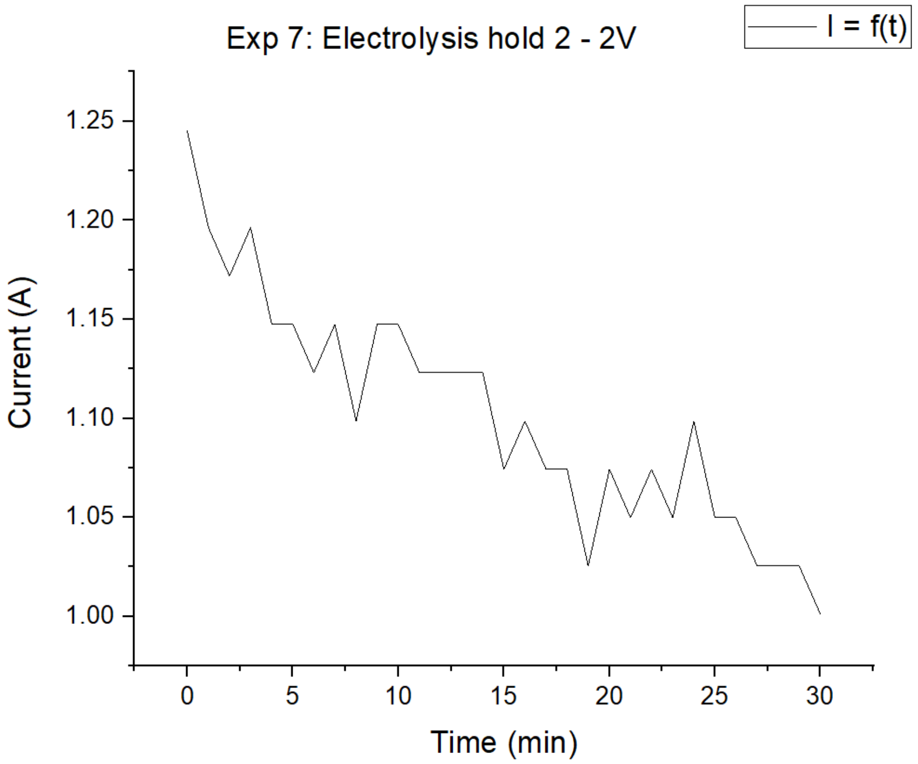

Figure 16: Current as a function of deposition time for electrolysis hold 2

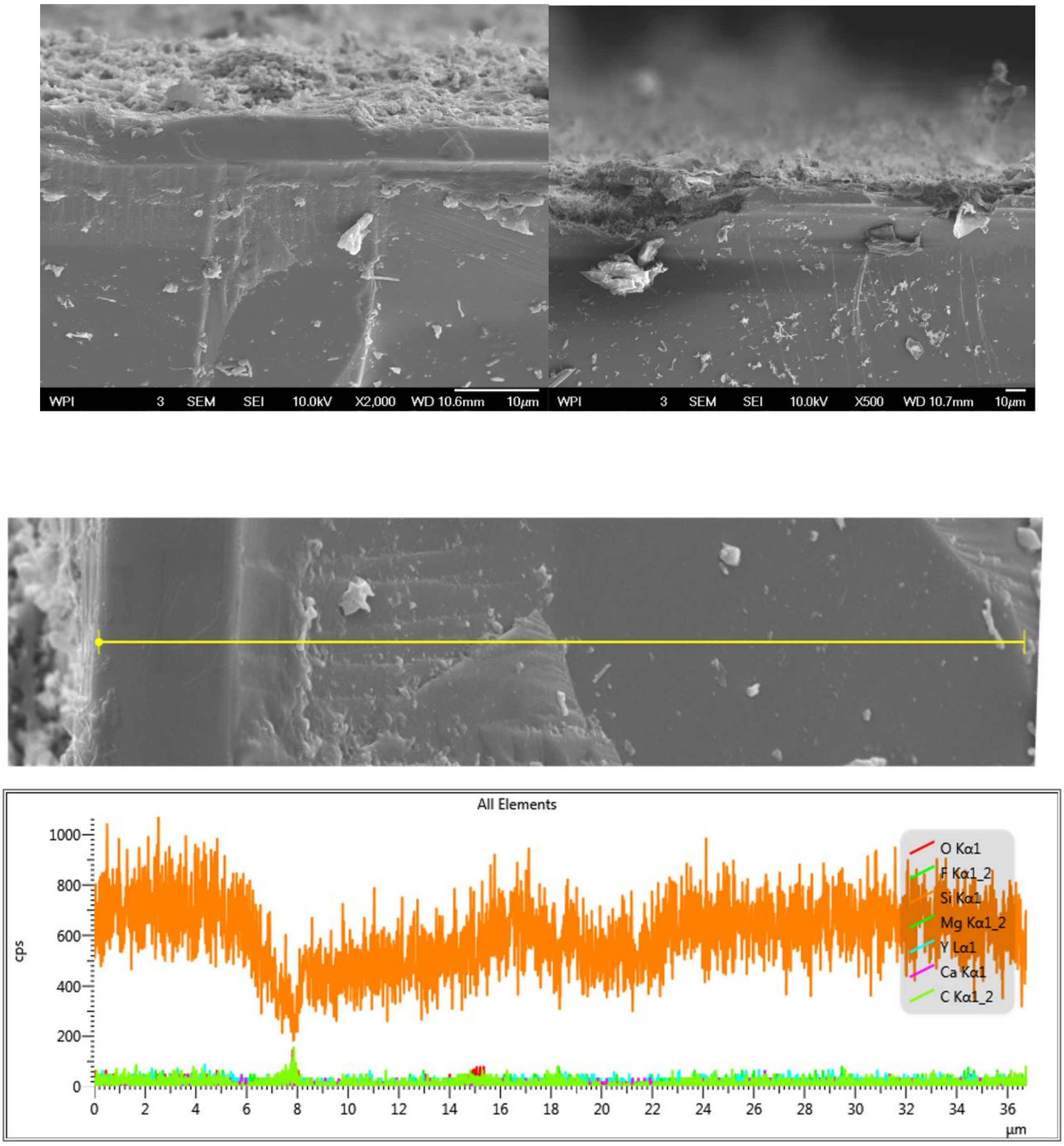

Figure 17: Scanning electron micrograph showing the edges of the sample (above) and an EDS line scan below showing composition and thickness of deposit.

Subsequent experiments used medical grade stainless beakers. A summary of subsequent experiments is given in the table below. Use of the stainless-steel beaker as a crucible caused Fe and Co to contaminate the flux and this is shown in the EDS scans in figure.

Experiment	Initial Conditions	Results
11	Si_3N_4 coated wafer	Test experiment. No electrolysis performed. No shrinkage in wafer
12	Si_3N_4 coated wafer	Wafer stuck in melt. Unable to characterise.
13	Si_3N_4 coated wafer	Furnace failure. Creep seen in wafer.
14	Si_3N_4 coated wafer	SOM tube cracked mid experiment. No current reading after 2 sweeps.
15	Switched to a thicker wafer to prevent bending and thinning of wafer.	Furnace failure. Switched to a different furnace.
16	Thicker wafer. New salt composition	SOM tube failure. No value of current
17	Boron Nitride coated steel crucible	Long electrolysis run. 7 hours. Pure silicon in melt.
18	Boron Nitride coated steel crucible. Use of a high-powered switch.	Pure silicon in melt
19	Boron Nitride coated steel crucible. Lower CaO salt composition	Pure silicon in melt
20	Boron Nitride coated steel crucible. Lower CaO salt composition. Use of a high-powered switch at lower duty cycle for a longer duration.	Pure silicon in melt

Table 5: Experimental summary of experiments 11- 20

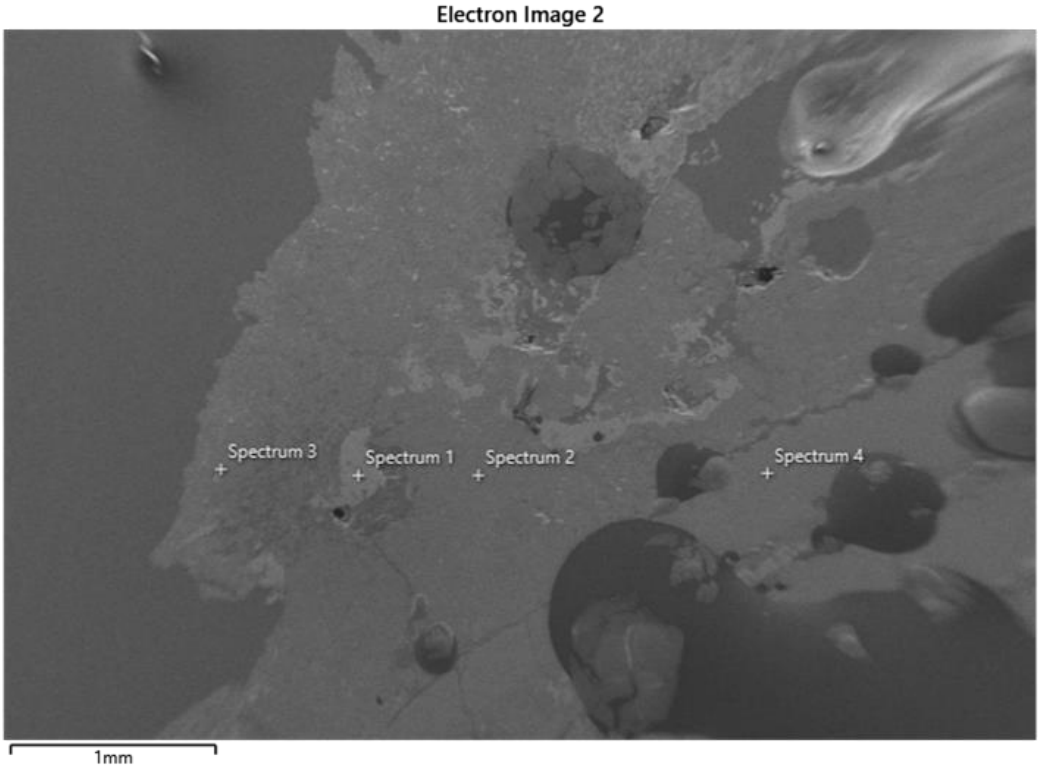

Figure 18: Point scan of sample showing regions chosen for compositional analysis of sample.

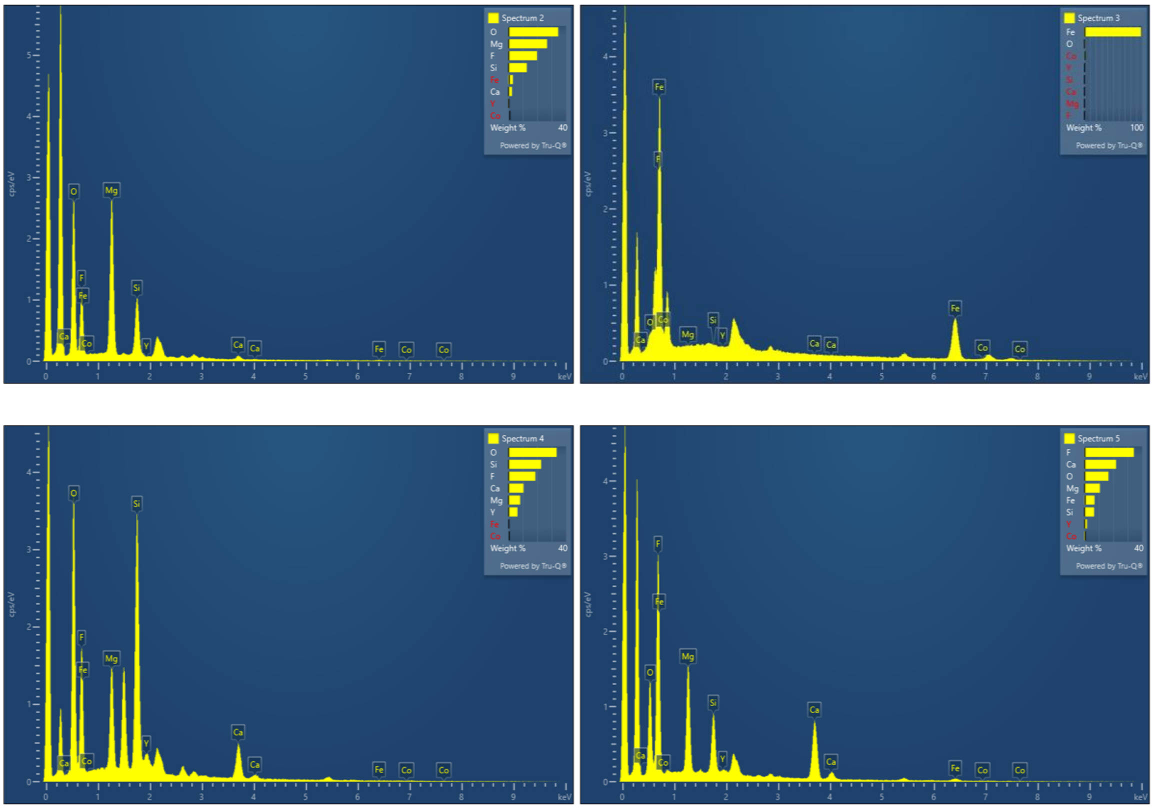

Figure 19: EDS compositional point scan showing Fe contamination in flux.

Experiment 18 showed pure silicon in the melt. There was no silicon adhering to the cathode. There was also the formation of MgO seen in the experiments. This is like the Pidgeon process where magnesium oxide is reduced to magnesium using ferrosilicon. This was overcome by reducing the wt.% of the CaO in the flux thus reducing the affinity of the magnesium ions to oxide ions.

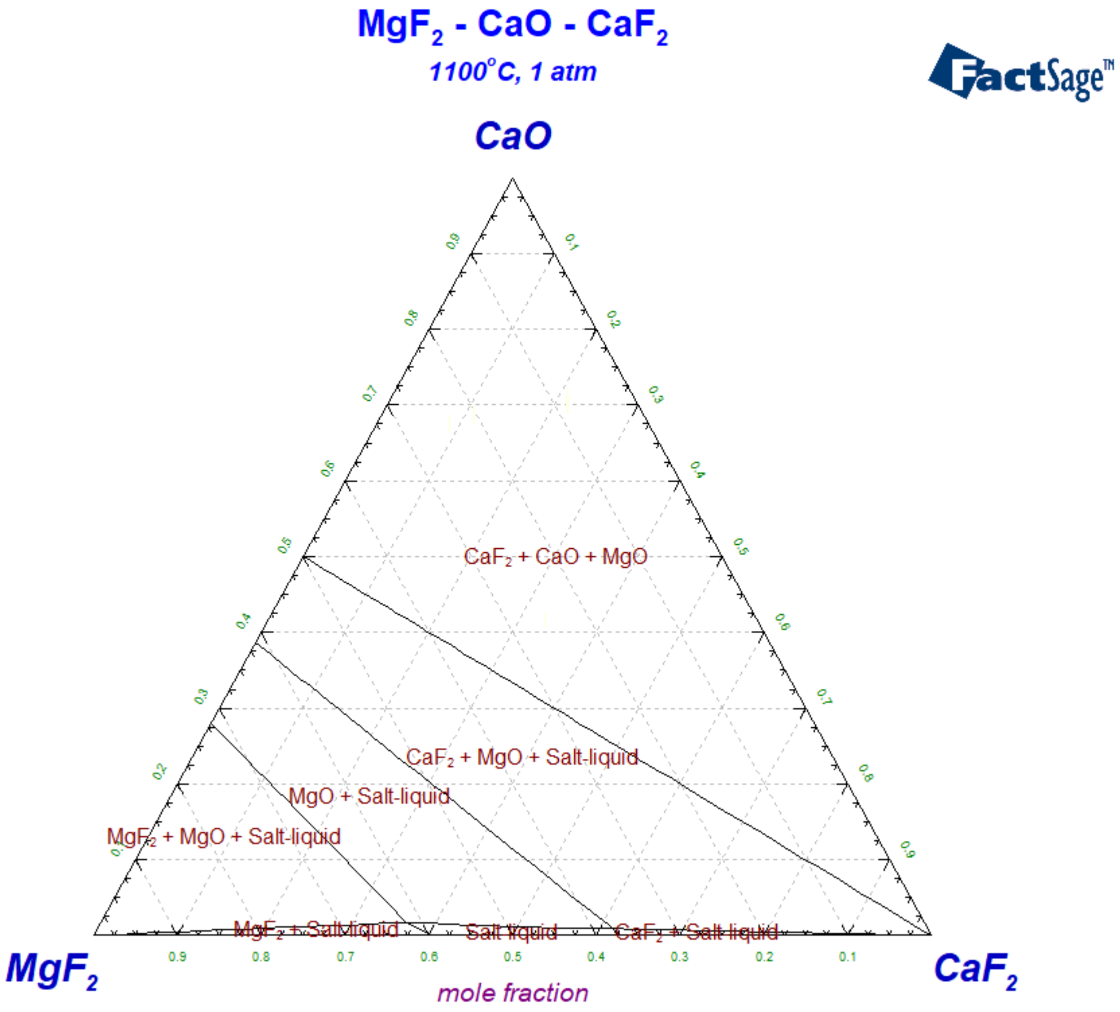

Figure 20: Ternary phase diagram showing formation of MgO at 1100^{0}C

The electrolysis scan below shows the current vs time graph for a long run electrolysis experiment nineteen. The salt composition had been changed to 39.74

wt.% MgF_2, 52.97 wt.% CaF_2, 1.69 wt.% CaO, 3.1 wt.% Y_2O_3, and 2.5 wt.% SiO_2. The corresponding EDS images follow showing pure silicon in the melt with the formation of MgO.

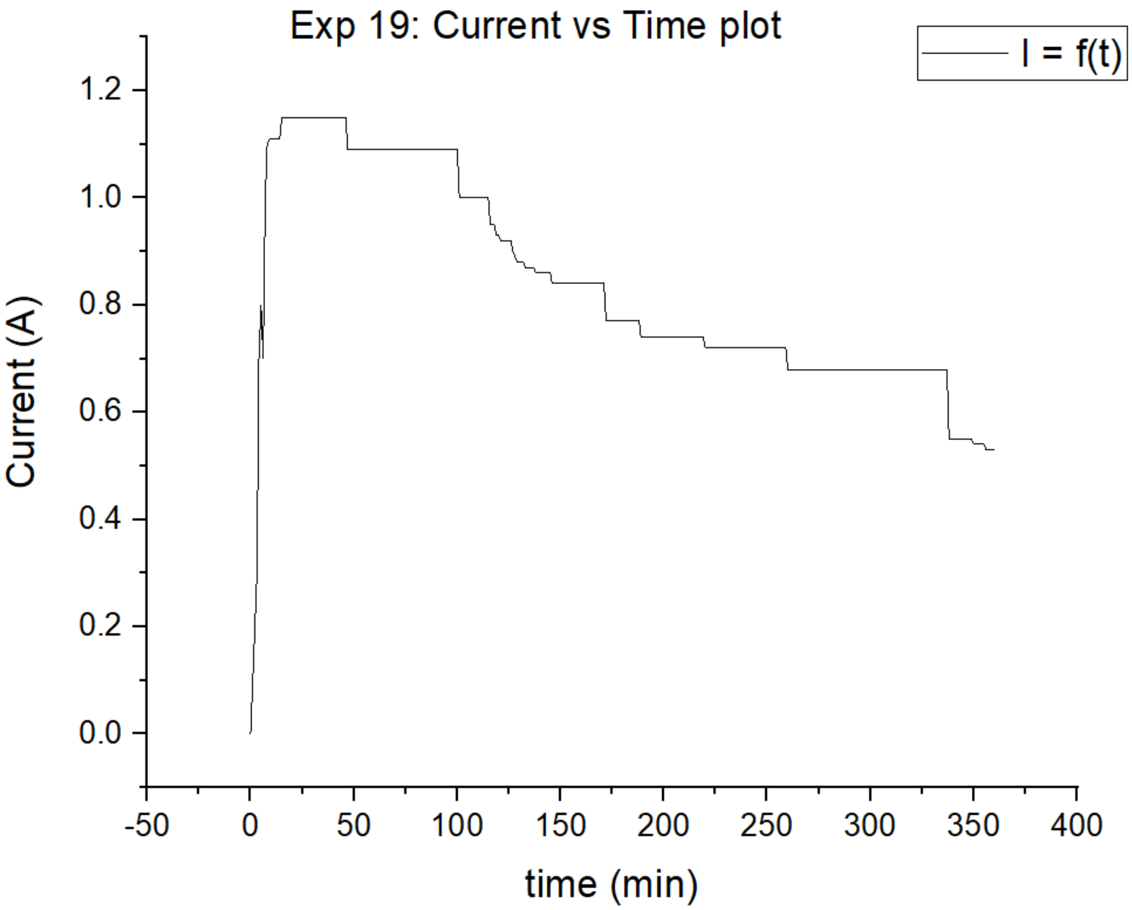

Figure 21: Current as a function of deposition time for long run electrolysis

A compositional scan of the sample shows good purity silicon in the melt. There are also traces of the other elements of the flux. We still see the formation of MgO but not a high percentage as before.

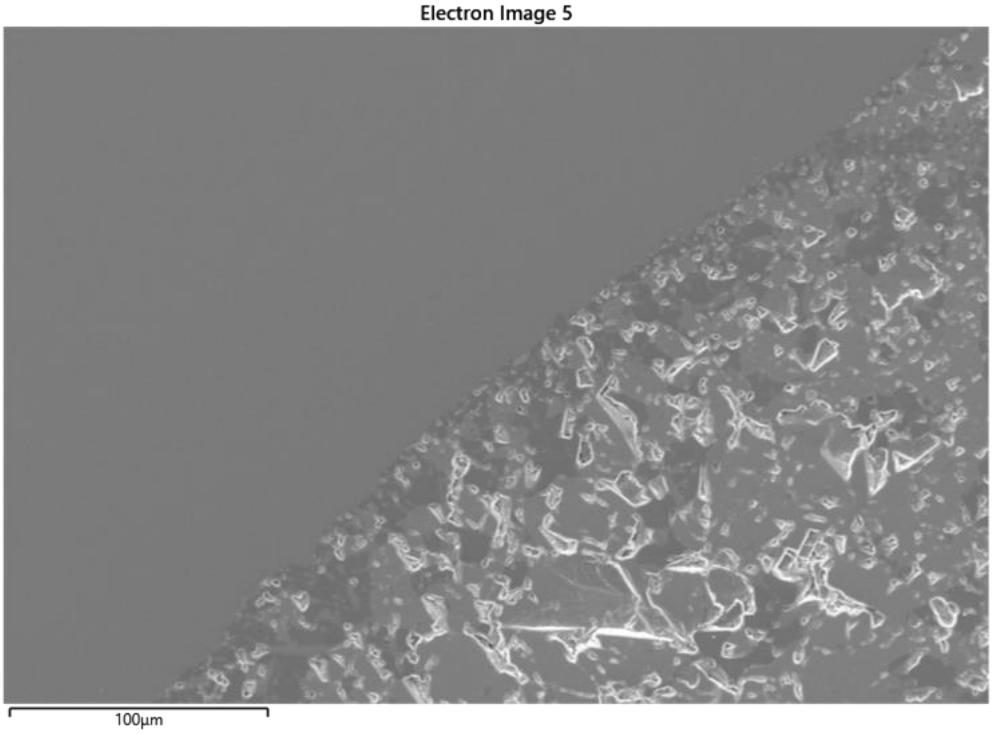

Figure 22: SEM image showing the flux and the wafer interface with Figure 23 (page 73) showing the complimentary EDS compositional map showing formation of MgO

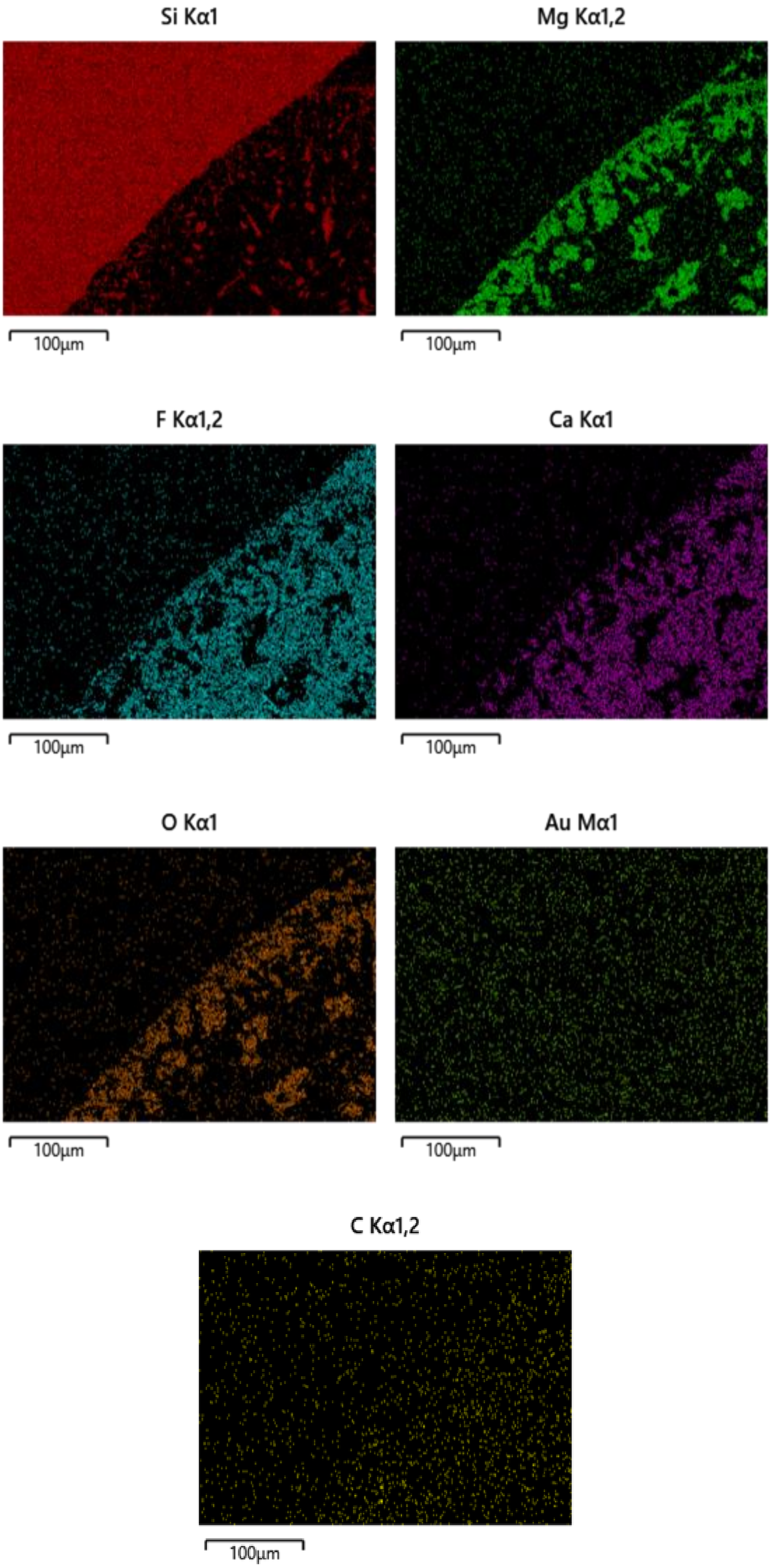

Figure 23: EDS compositional map showing formation of MgO

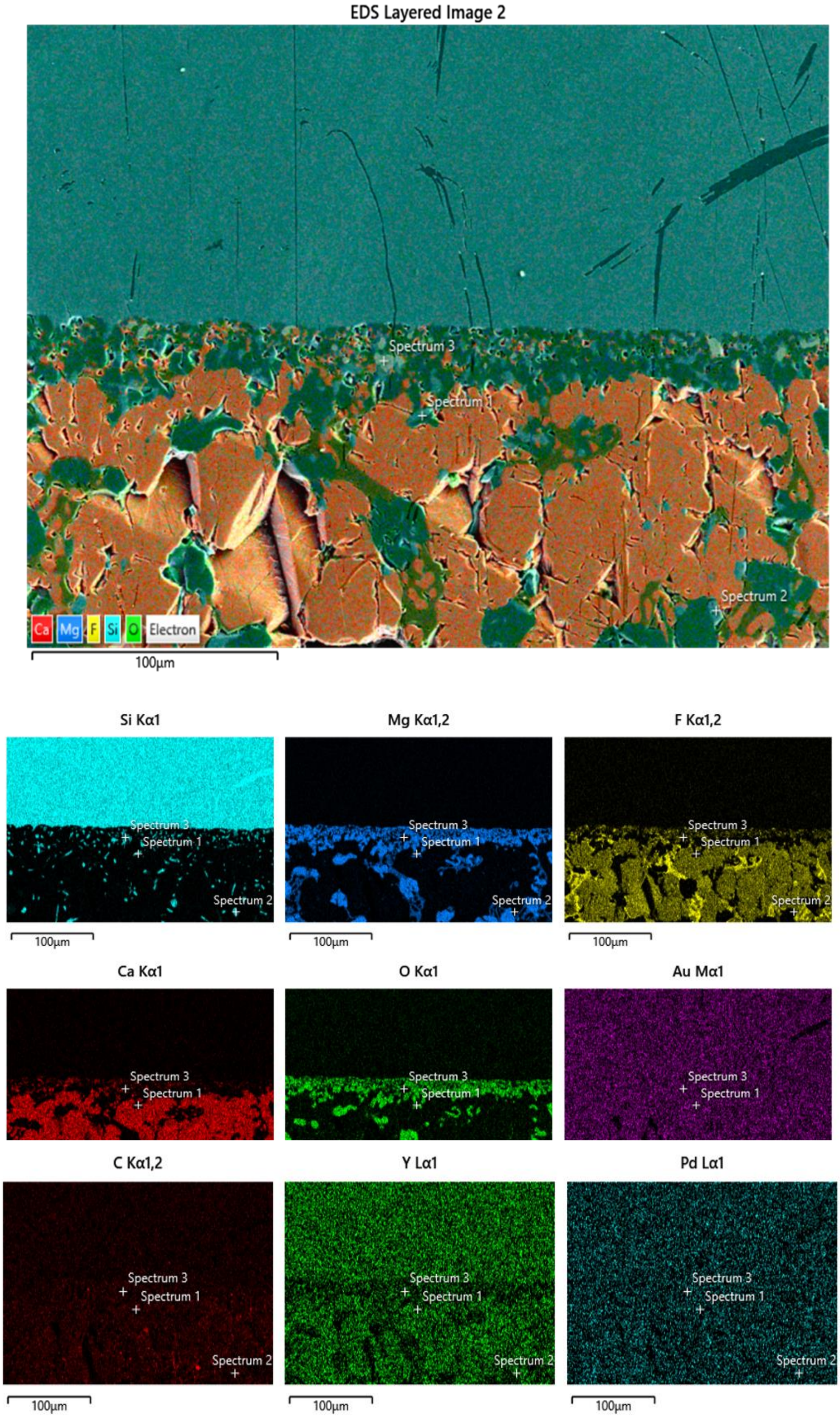

Figure 24: EDS compositional map showing pure silicon in flux with lower CaO flux.

4.4 Results and Discussions

In conclusion, the series of twenty experiments conducted with the aim of obtaining silicon deposits on the cathode in the molten salt electrolyte system used did not yield the desired results. Despite the numerous trials, pure silicon was seen in the melt, but no silicon deposits were observed on the cathode, indicating that the experimental conditions or parameters may require further optimization or reconsideration.

Several factors could be responsible for the absence of silicon deposits in these experiments, including the weights of each component of the electrolyte composition, applied voltage, cathode material, or the presence of impurities. It is possible that the chosen molten salt did not provide sufficient ionic conductivity or that the silicon ions were hindered from migrating towards the cathode. Alternatively, the experimental conditions may have promoted some side reactions, and mass-transfer limiting conditions preventing silicon deposition.

An additional aspect to consider is the use of a high-powered switch to reverse potentials in the system. The purpose of this switch is to prevent dendrite formation, which could potentially cause short-circuiting and other issues in the cell. By periodically reversing the potential, it may be possible to limit dendrite growth and promote more uniform silicon deposition on the cathode.

A notable observation during the electrolysis experiments was the discoloration of the flux. It is hypothesized that this phenomenon may be attributed to the solubility of metal ions in the flux, as illustrated in the accompanying figure. Further investigation is required to elucidate the underlying mechanisms and potential implications.

Figure 25: Discoloration of flux observed following the electrolysis process.

To improve the outcomes of future experiments, a systematic investigation of the various parameters and their effects on the silicon deposition process should be conducted. This may include exploring alternative electrolyte compositions, adjusting the temperature or voltage, using a different cathode material, or implementing the high-powered switch to reverse potentials as a means of managing dendrite formation. Additionally, rigorous control of oxides and experimental conditions may be necessary to eliminate potential sources of interference like the formation of MgO.

Chapter 5 - Conclusions and Future Work

5.1 Conclusions

This project successfully demonstrated the production of high-purity silicon using a molten salt electrolyte through a systematic approach. The study achieved primary, secondary, and tertiary current distribution, which provided valuable insights into the electrochemical behaviour of the system and the silicon deposition process. The experimental results have highlighted the effectiveness of the molten salt electrolysis technique in producing high-quality silicon for various applications, especially the solar industries.

The primary, secondary, and tertiary current distributions played an important role in understanding the intricacies of the electrolysis process. These findings provided a strong foundation for optimising the cell design, electrode geometry, and electrolyte composition to enhance the efficiency and product quality of the silicon deposition process. Furthermore, the successful achievement of high-purity silicon has emphasised the potential of this technique as a promising alternative to conventional silicon production methods.

For future work, the implementation of phase field modelling could offer significant advantages in understanding and optimising the silicon electrodeposition process. Phase field modelling is a powerful computational tool capable of simulating complex microstructural evolution and predicting the formation of dendrites, which are common challenges in electrodeposition processes. By incorporating phase field modelling into the research, it would be possible to gain a deeper understanding of the nucleation and growth mechanisms of silicon during the electrodeposition process and prevent short circuiting of the cell.

This advanced modelling technique would allow for the optimization of critical process parameters, such as current density, electrolyte composition, and temperature, to minimise dendritic growth and improve the overall quality of the deposited silicon. Additionally, phase field modelling could also provide valuable information on the effects of various electrode geometries and cell designs on the electrochemical behaviour of the system, enabling further optimization of the deposition process through introducing vorticity at the mesoscale level.

In summary, the successful production of high-purity silicon in a molten salt electrolyte and the achievement of primary, secondary, and tertiary current distributions have laid a solid foundation for further research and development in this field. The incorporation of phase field modelling in future work would offer a comprehensive understanding of the silicon electrodeposition process, leading to enhanced efficiency, product quality, and scalability of the molten salt electrolysis technique for silicon production.

Bibliography

Bøe, G., Grjotheim, K., Matiašovský, K., & Fellner, P. (1971). Electrolytic deposition of silicon and of silicon alloys Part III: Deposition of silicon and aluminum using a copper cathode. *Canadian Metallurgical Quarterly*, *10*(4), 281–285. https://doi.org/10.1179/cmq.1971.10.4.281

Bøe, G., Grjotheim, K., Matiašovský, K., & Fellner, P. (1972). Electrolytic deposition of silicon and of silicon alloys. Part IV: Preparation of alloys with a high content of silicon, and silicon refining. *Canadian Metallurgical Quarterly*, *11*(3), 463–467. https://doi.org/10.1179/cmq.1972.11.3.463

Buasai, S., McMahon, A., & Wu, Y. J. (2020). *Solar Silicon Epitaxy by Molten Salt Electrolysis* [Major Qualifying Project]. Worcester Polytechnic Institute.

Building a Magnetohydrodynamic Multiphysics Model in COMSOL® | COMSOL Blog. (n.d.). Retrieved April 5, 2023, from https://www.comsol.com/blogs/building-a-magnetohydrodynamic-multiphysics-model-in-comsol/

Chase, M. W. (1996). *NIST-JANAF Thermochemical Tables* (Fourth Edition) [Data set]. National Institute of Standards and Technology. https://doi.org/10.18434/T42S31

Chigondo, F. (2018). From Metallurgical-Grade to Solar-Grade Silicon: An Overview. *Silicon*, *10*(3), 789–798. https://doi.org/10.1007/s12633-016-9532-7

Cohen, U. (1977). Some prospective applications of silicon electrodeposition from molten fluorides to solar cell fabrication. *Journal of Electronic Materials*, *6*(6), 607–643. https://doi.org/10.1007/BF02660341

Elwell, D., & Rao, G. M. (1988). Electrolytic production of silicon. *Journal of Applied Electrochemistry*, *18*(1), 15–22. https://doi.org/10.1007/BF01016199

Grjotheim, K., Matiaśovský, K., Fellner, P., & Silný, A. (1971). Electrolytic deposition of silicon and of silicon alloys Part I: Physicochemical properties of the Na_3AlF_6-Al_2O_3-SiO_2 mixtures. *Canadian Metallurgical Quarterly*, *10*(2), 79–82. https://doi.org/10.1179/cmq.1971.10.2.79

Guan, X., Pal, U. B., Gopalan, S., & Powell, A. C. (2013). LSM ($La_{0.8}Sr_{0.2}0.2MnO_{3-\delta}$)–Inconel Inert Anode Current Collector for Solid Oxide Membrane (SOM) Electrolysis. *Journal of The Electrochemical Society*, *160*(11), F1179–F1186. https://doi.org/10.1149/2.016311jes

Haarberg, G. M., Kato, T., Norikawa, Y., & Nohira, T. (2019a). Electrodeposition of Silicon with a Liquid Gallium Cathode in Molten Salts. *ECS Transactions*, *89*(7), 29. https://doi.org/10.1149/08907.0029ecst

Haarberg, G. M., Kato, T., Norikawa, Y., & Nohira, T. (2019b). Electrodeposition of Silicon with a Liquid Gallium Cathode in Molten Salts. *ECS Transactions*, *89*(7), 29–35. https://doi.org/10.1149/08907.0029ecst

Hazerjian, J. M., Luu, V., & Ly, A. (2021). *Solar-Grade Silicon: Techno-economic Assessment, COMSOL Modeling, and Electrolysis* [Major Qualifying Project]. Worcester Polytechnic Institute. https://digitalwpi.wpi.edu/concern/student_works/zs25xc44f

Ibl, N. (1983). Current Distribution. In E. Yeager, J. O. Bockris, B. E. Conway, & S. Sarangapani (Eds.), *Comprehensive Treatise of Electrochemistry: Electrodics: Transport* (pp. 239–315). Springer US. https://doi.org/10.1007/978-1-4615-6690-8_4

Jin, X., Gao, P., Wang, D., Hu, X., & Chen, G. Z. (2004). Electrochemical Preparation of Silicon and Its Alloys from Solid Oxides in Molten Calcium Chloride. *Angewandte Chemie International Edition*, *43*(6), 733–736. https://doi.org/10.1002/anie.200352786

Juzeliunas, E. (2022). *Silicon: Electrochemistry, Production, Purification and Applications* (1st edition). Wiley-VCH.

Krishnan, A. (2006). *Solid Oxide Membrane Process for the Direct Reduction of Magnesium from Magnesium Oxide* [Ph.D.]. Boston University.

Kvande, H. (2014). The Aluminum Smelting Process. *Journal of Occupational and Environmental Medicine*, *56*, S2. https://doi.org/10.1097/JOM.0000000000000154

Ma, Y., Ido, A., Yasuda, K., Hagiwara, R., Homma, T., & Nohira, T. (2019). Mechanism of

Electrolytic Reduction of SiO_2 at Liquid Zn Cathode in Molten $CaCl_2$. *Journal of The Electrochemical Society*, *166*(6), D162–D167. https://doi.org/10.1149/2.1211904jes

Maldonado, S. (2020). The Importance of New “Sand-to-Silicon” Processes for the Rapid Future Increase of Photovoltaics. *ACS Energy Letters*, *5*(11), 3628–3632. https://doi.org/10.1021/acsenergylett.0c02100

Matuszak, D. (2013). *ARPA-E METALS Tool* (1.0) [Microsoft Excel Spreadsheet]. Unpublished, Distributed to U.S. Department of Energy Grantees.

Maurits, J. E. A. (2014). Chapter 2.6—Silicon Production. In S. Seetharaman (Ed.), *Treatise on Process Metallurgy* (pp. 919–948). Elsevier. https://doi.org/10.1016/B978-0-08-096988-6.00022-5

Monnier, R., & Giacometti, J. C. (1964). Recherches sur le raffinage électrolytique du silicium. *Helvetica Chimica Acta*, *47*(2), 345–353. https://doi.org/10.1002/hlca.19640470202

Moore, J. T., Wang, T. H., Heben, M. J., Douglas, K., & Ciszek, T. F. (1997). Fused-salt electrodeposition of thin-layer silicon. *Conference Record of the Twenty Sixth IEEE Photovoltaic Specialists Conference - 1997*, 775–778. https://doi.org/10.1109/PVSC.1997.654204

Moudgal, A., Buasai, S., Wu, Y. J., McMahon, A., Hazerjian, J., Luu, V., Ly, A., Asadikiya, M., Powell, A., Pal, U., & Zhong, Y. (2021). Finite Element Analysis and Techno-Economic Modeling of Solar Silicon Molten Salt Electrolysis. *JOM*, *73*(1). https://doi.org/10.1007/s11837-020-04468-y

Nohira, T. (2014). Silicon Production by Molten Salt Electrolysis. In G. Kreysa, K. Ota, & R. F. Savinell (Eds.), *Encyclopedia of Applied Electrochemistry* (pp. 1963–1966). Springer New York. https://doi.org/10.1007/978-1-4419-6996-5_457

Oishi, T., Watanabe, M., Koyama, K., Tanaka, M., & Saegusa, K. (2011). Process for Solar Grade Silicon Production by Molten Salt Electrolysis Using Aluminum-Silicon Liquid Alloy. *Journal of The Electrochemical Society*, *158*(9), E93. https://doi.org/10.1149/1.3605720

Osborne, M. (2014, January 9). Explosion at Mitsubishi polysilicon plant in Japan causes deaths. *PV Tech*. https://www.pv-tech.org/news/explosion_at_mitsubishi_polysilicon_plant_in_japan_causes_deaths

Padamata, S. K., & Saevarsdottir, G. (2023). Silicon electrowinning by molten salts electrolysis. *Frontiers in Chemistry*, *11*, 1133990. https://doi.org/10.3389/fchem.2023.1133990

Pal, U. B., & Powell, A. C. (2007). The use of solid-oxide-membrane technology for electrometallurgy. *JOM*, *59*(5), 44–49. https://doi.org/10.1007/s11837-007-0064-x

Photovoltaics Report—Fraunhofer ISE. (n.d.). Fraunhofer Institute for Solar Energy Systems ISE. Retrieved April 4, 2023, from https://www.ise.fraunhofer.de/en/publications/studies/photovoltaics-report.html

Polysilicon price reaches $39.3/kg—The highest since 2011. (2022, February 23). Pv Magazine USA. https://pv-magazine-usa.com/2022/02/23/polysilicon-price-reaches-39-3-kg-the-highest-since-2011/

Powell, A., & Pati, S. (2012). Multi-Physics Modeling of Molten Salt Transport in Solid Oxide Membrane (SOM) Electrolysis and Recycling of Magnesium. In L. Nastac, L. Zhang, B. G. Thomas, A. Sabau, N. El-Kaddah, A. C. Powell, & H. Combeau (Eds.), *CFD Modeling and Simulation in Materials Processing* (pp. 57–64). John Wiley & Sons, Inc. https://doi.org/10.1002/9781118364697.ch7

Solar Manufacturing Cost Analysis. (n.d.). Retrieved April 4, 2023, from https://www.nrel.gov/solar/market-research-analysis/solar-manufacturing-cost.html

Solar Photovoltaic Cell Basics. (n.d.). Energy.Gov. Retrieved April 4, 2023, from https://www.energy.gov/eere/solar/solar-photovoltaic-cell-basics

Spatocco, B., & Sadoway, D. (2015). *Cost-Based Discovery for Engineering Solutions* (pp. 227–262). https://doi.org/10.1002/9783527690633.ch7

Stinn, C., & Allanore, A. (2020). Estimating the Capital Costs of Electrowinning Processes. *Electrochemical Society Interface*, *29*(2), 44–49. https://doi.org/10.1149/2.F06202IF

Vatalis, K. I., Charalambides, G., & Benetis, N. P. (2015). Market of High Purity Quartz

Innovative Applications. *Procedia Economics and Finance*, *24*, 734–742. https://doi.org/10.1016/S2212-5671(15)00688-7

Villalón Jr, T. (2018). *Zero-Direct Emission Silicon Production via Solid Oxide Membrane Electrolysis* [Ph.D., Boston University]. https://hdl.handle.net/2144/30729

Wilson, G. M., Al-Jassim, M., Metzger, W. K., Glunz, S. W., Verlinden, P., Xiong, G., Mansfield, L. M., Stanbery, B. J., Zhu, K., Yan, Y., Berry, J. J., Ptak, A. J., Dimroth, F., Kayes, B. M., Tamboli, A. C., Peibst, R., Catchpole, K., Reese, M. O., Klinga, C. S., … Sulas-Kern, D. B. (2020). The 2020 photovoltaic technologies roadmap. *Journal of Physics D: Applied Physics*, *53*(49), 493001. https://doi.org/10.1088/1361-6463/ab9c6a

Woodhouse, M. A., Smith, B., Ramdas, A., & Margolis, R. M. (2019). *Crystalline Silicon Photovoltaic Module Manufacturing Costs and Sustainable Pricing: 1H 2018 Benchmark and Cost Reduction Road Map* (NREL/TP-6A20-72134, 1495719; p. NREL/TP-6A20-72134, 1495719). https://doi.org/10.2172/1495719

Yasuda, K., & Nohira, T. (2022). Electrochemical production of silicon. *High Temperature Materials and Processes*, *41*(1), 247–278. Scopus. https://doi.org/10.1515/htmp-2022-0033

Yasuda, K., Nohira, T., Amezawa, K., Ogata, Y. H., & Ito, Y. (2005). Mechanism of Direct Electrolytic Reduction of Solid SiO_2 to Si in Molten $CaCl_2$. *Journal of The Electrochemical Society*, *152*(4), D69. https://doi.org/10.1149/1.1864453